IJMMM International Journal of Minerals, Metallurgy and Materials 矿物冶金与材料学报（英文版）

In-situ observation of nonmetallic inclusions in steel using confocal scanning laser microscopy: A review

Ying Ren and Lifeng Zhang

Cite this article as:
Ying Ren and Lifeng Zhang, *In-situ* observation of nonmetallic inclusions in steel using confocal scanning laser microscopy: A review, *Int. J. Miner. Metall. Mater.*, 32(2025), No. 5, pp. 975-991. https://doi.org/10.1007/s12613-025-3103-0

View the article online at SpringerLink or IJMMM Webpage.

INTERNATIONAL JOURNAL OF
Minerals, Metallurgy and Materials

Volume 32, Number 5, May 2025
Page 975

Review https://doi.org/10.1007/s12613-025-3103-0

In-situ observation of nonmetallic inclusions in steel using confocal scanning laser microscopy: A review

Ying Ren[1)] *and Lifeng Zhang*[2),✉]

1) School of Metallurgical and Ecological Engineering, University of Science and Technology Beijing, Beijing 100083, China
2) School of Mechanical and Materials Engineering, North China University of Technology, Beijing 100144, China
(Received: 19 November 2024; revised: 25 January 2025; accepted: 27 January 2025)

Abstract: The characteristics of nonmetallic inclusions formed during steel production have a significant influence on steel performance. In this paper, studies on inclusions using confocal scanning laser microscopy (CSLM) are reviewed and summarized, particularly the collision of various inclusions, dissolution of inclusions in liquid slag, and reactions between inclusions and steel. Solid inclusions exhibited a high collision tendency, whereas pure liquid inclusions exhibited minimal collisions because of the small attraction force induced by their <90° contact angle with molten steel. The collision of complex inclusions in molten steel was not included in the scope of this study and should be evaluated in future studies. Higher CaO/Al_2O_3 and CaO/SiO_2 ratios in liquid slag promoted the dissolution of Al_2O_3-based inclusions. The formation of solid phases in the slag should be prevented to improve dissolution of inclusions. To accurately simulate the dissolution of inclusions in liquid slag, *in-situ* observation of the dissolution of inclusions at the steel–slag interface is necessary. Using a combination of CSLM and scanning electron microscopy–energy dispersive spectroscopy, the composition and morphological evolution of the inclusions during their modification by the dissolved elements in steel were observed and analyzed. Although the *in-situ* observation of MnS and TiN precipitations has been widely studied, the *in-situ* observation of the evolution of oxide inclusions in steel during solidification and heating processes has rarely been reported. The effects of temperature, heating and cooling rates, and inclusion characteristics on the formation of acicular ferrites (AFs) have been widely studied. At a cooling rate of 3–5 K/s, the order of AF growth rate induced by different inclusions, as reported in literature, is Ti–O < Ti–Ca–Zr–Al–O < Mg–O < Ti–Zr–Al–O < Mn–Ti–Al–O < Ti–Al–O < Zr–Ti–Al–O. Further comprehensive experiments are required to investigate the quantitative relationship between the formation of AFs and inclusions.

Keywords: inclusion; steel; *in-situ* observation; confocal scanning laser microscopy

1. Introduction

The formation of nonmetallic inclusions during production of high-quality steels is a significant issue. Steel performance is related to quantity, size, composition, and distribution of such inclusions. The characteristics of these inclusions evolve during steel processing; for example, nucleation and collision occur after deoxidation during converter tapping [1–3]. During the refining process, inclusions float to the surface of the molten steel [4–6] and are dissolved in the refining slag [7–9]. Additionally, alloy treatment [10–13] and slag modification [14–16] can modify inclusion composition. Moreover, reoxidation and slag entrainment can be prevented to improve steel cleanliness [17–19]. The inclusion behavior during steelmaking, refining, and continuous casting processes, which cannot be directly observed because of the high temperature of molten steel, must be investigated.

Confocal scanning laser microscopy (CSLM) combines advanced technologies such as infrared heating, high-temperature stretching and compression, and confocal laser scanning. A schematic of CSLM equipment is shown in Fig. 1 [20]. The surface of samples can be observed *in-situ* under different conditions of temperature and pressure. CSLM is widely used in industries such as welding, materials, and metallurgy for purposes such as *in-situ* observation of the formation of acicular ferrites (AFs) induced by oxide metallurgy [21], phase transformation during cooling and heating of materials [22–23], and metal solidification and inclusion evolution on the surface of liquid metals [24–25].

In the 1950s, Minsky proposed the basic concept of confocal microscopy and applied it to technical patents. In the 1990s, the rapid development of optical, electronic, and computer technologies promoted the development and application of CSLM, which is commonly used to observe micromorphology [26]. Chikama *et al.* [27] used a laser beam and infrared furnace to observe the dynamics of crystal growth in iron–carbon melts; CSLM has since been widely used in the study of steel. Particularly, CSLM has been widely applied for the *in-situ* observation of inclusion behaviors on molten steel surfaces. In 1997, Yin's group [28–29] used CSLM to

✉ Corresponding author: Lifeng Zhang E-mail: zhanglifeng@ncut.edu.cn

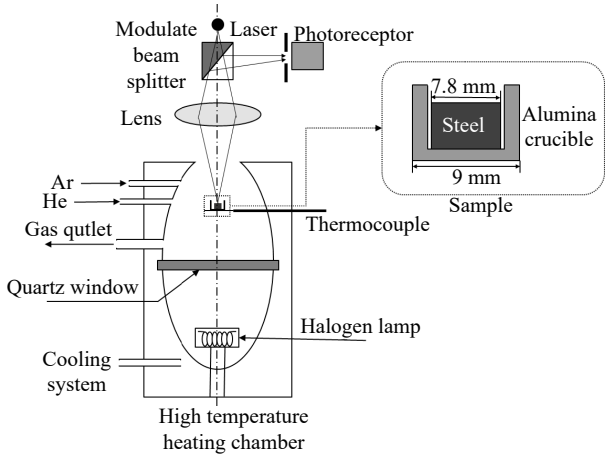

Fig. 1. Schematic of CSLM equipment [20]. Reprinted by permission from Springer Nature: *Metall. Mater. Trans. B*, *In situ* observation of the agglomeration of MgO–Al_2O_3 inclusions on the surface of a molten GCr15-bearing steel, M.H. Wu, C.Y. Ren, Y. Ren, and L.F. Zhang, Copyright 2023.

observe the collision of different inclusions on the surface of molten steel. In 1998, Shibata *et al.* [30] observed the engulfment and pushing of inclusions in molten steel at the melt–solid interface using CSLM. In 1999, Hanamura *et al.* [31] used CSLM for the *in-situ* observation of the influence of inclusions on ferrite formation. In 2000, Sridhar and Cramb [32] used CSLM to study the dissolution of Al_2O_3 inclusion particles in Al_2O_3–SiO_2–CaO–MgO slags at 1430–1550°C. In 1998, Yuki *et al.* [24] observed the precipitation of MnS inclusions in Fe–42wt%Ni using CSLM. In 2017, Khurana *et al.* [33] observed the modification of inclusions by calcium treatment using CSLM. Thus, by combining *in-situ* observation and temperature simulation of the steel production process, CSLM can effectively monitor the evolution of inclusions in molten steel.

2. *In-situ* observation of the collision of inclusions in steel

In recent years, researchers have conducted numerous CSLM experiments on the collision of inclusions, including Al_2O_3 [28–29,34], 80wt% Al_2O_3–20wt% SiO_2 [28,35], MgO [36], 93wt% Al_2O_3–7wt% MgO [36–37], Al_2O_3–CaO–SiO_2 [38], Al_2O_3–CaO [28,33,39–41], CaO–MgO–Al_2O_3 [38], CaO–MgO–Al_2O_3–SiO_2 [35,42], Al_2O_3–Ce_2O_3 [43–44], Ce_2O_2S [45], SiO_2 [46], TiN [25–27], MnS [47–49], and Ti_2O_3 [50]. Primary interfaces include steel–slag interface [33,39–42,50–51], steel–Ar interface [28,34,36,50–55], solid–liquid interface [37,39,56], and slag surface [40]. Table 1 summarizes related studies on the observation of inclusion collision using CSLM [25,28–29,34–40,45,47,50,53,56–63].

The collisions of inclusions are related to their liquid fractions. The inclusion composition in steel samples before the CSLM experiments was analyzed using scanning electron microscopy–energy dispersive spectroscopy (SEM–EDS). The melting temperature was calculated using the FactSage software to evaluate the solid and liquid inclusions. As shown in Fig. 2(a) [28], Yin reported that solid inclusions, such as Al_2O_3, exhibited a significant attractive force and had a high tendency to collide. However, pure liquid inclusions such as CaO–Al_2O_3 rarely collided because of their small mutual attraction. The collision between inclusions was due to the long-range attractive force between solid particles on the steel surface, which was caused by capillary action [64]. Fig. 2(b) [60] shows that there is no significant collision of liquid inclusions. Fig. 3 shows the variation in attractive force between inclusions at different distances [28,36–38,44,46,52]. R_1 and R_2 denote the radii of the two inclusions. Capillary force between inclusions was primarily influenced by the contact angle between the inclusions and steel, as well as surface tension and density of molten steel. Because surface tension and density of molten steel changed minimally during steelmaking, the capillary force of the inclusions was primarily related to the contact angle between the inclusions and steel. The order of capillary force for different inclusions was Al_2O_3 > $TiAlO_x$–Al_2O_3 > Ce_2O_3 > Ce–Al–O > Al_2O_3–SiO_2 > Ce–O–S > Al_2O_3–CaO > SiO_2 > MgO > $MgAl_2O_4$; this was positively correlated with the change in contact angles between the inclusions and steel [65]. Notably, attraction between inclusions refers to that between inclusions of the same type. For instance, the attraction between Al_2O_3–SiO_2 composite inclusions refers to the attraction between one or more Al_2O_3–SiO_2 composite inclusions. Previous investigations primarily focused on the collision of inclusions at the steel–Ar interface, and the collision of inclusions at the steel–slag interface has become more complex. Both long-range attractive and repulsive forces acted when the distance between two inclusions was less than 100–150 μm [39]. Liquid Al_2O_3–CaO inclusions rarely collided at the steel–slag interface, and the collision ability of the inclusions significantly increased [40].

The capillary force between inclusions under various physical and chemical conditions was calculated according to the attractive capillary force model [53], as shown in Fig. 4. According to Fig. 4(a) and (b), the attractive capillary force exhibits a positive correlation with the density and size of the inclusions. The larger the density and size of the inclusions, the greater the capillary force on the surface of molten steel. The dependence of the capillary forces on contact angle is shown in Fig. 4(c) [53]. The attractive capillary force first decreased and then increased and was very close to zero at a contact angle of 90°. The correlation between surface tension of liquid steel and capillary suction force is shown in Fig. 4(d) [53]. When surface tension decreased from 1.9 to 1.1 J/m^2, the attractive capillary force increased slightly, leading to collisions of inclusions.

3. *In-situ* observation of the dissolution of inclusions in slag

In 2000, Sridhar and Cramb [32] *in-situ* observed the dissolution of Al_2O_3 inclusions in CaO–MgO–SiO_2–Al_2O_3 slag using CSLM, as shown in Fig. 5. The inclusion particles in previous studies were primarily pure oxides such as Al_2O_3,

Table 1. Studies on the observation of inclusion collisions using CSLM [25,28–29,34–40,45,47,50,53,56–63]

Authors	Year	Interface	Inclusion composition	Inclusion density / ($kg \cdot m^{-3}$)	Inclusion size / μm	Capillary attraction / N	Refs.
Yin *et al.*	1997	Steel–Ar	Al_2O_3	3900	10	10^{-16}	[28–29]
			Al_2O_3	3900	2		[34]
			80wt%Al_2O_3–SiO_2	3378	1–3	7.0×10^{-16}	[28,34]
			CaO–60wt%Al_2O_3–SiO_2		5–10	Noncollision	[34]
			CaO–80wt%Al_2O_3–SiO_2		1–3	4.0×10^{-16}	[34]
			CaO–Al_2O_3–95wt%SiO_2		5–10	8.2×10^{-15}	[34]
			CaO–50wt%Al_2O_3–SiO_2		5–10	Noncollision	[34]
			CaO–80wt%Al_2O_3	3768	3–5	6.5×10^{-14}	[34]
			CaO–60wt%Al_2O_3	3645	5–10	10^{-16}	[34]
			CaO·Al_2O_3		5–10	Noncollision	[34]
Kimura *et al.*	2000 2001	Steel–Ar	Al_2O_3·MgO	3600	5.3	5.0×10^{-18}– 5.0×10^{-16}	[36–37]
Kimura *et al.*	2001	Steel–Ar	MgO	3580			[36]
Nakajima and Mizoguchi	2001	Steel–Ar	30wt%CaO–60wt%Al_2O_3– 10wt%MgO		1.5–15.5	10^{-14}–10^{-17}	[38]
Nakajima and Mizoguchi	2001	Steel–Ar	40wt%CaO–55wt%Al_2O_3– 5wt%MgO		<40	Noncollision	[38]
Hasegawa *et al.*	2001	Steel–Ar	MnS		1–10	Noncollision	[47]
Vantilt *et al.*	2004	Steel–Ar	Al_2O_3–MnO–SiO_2		10	Noncollision	[51]
Wikstrom *et al.*	2008	Slag–Ar	CaO·Al_2O_3				[39]
Wikstrom *et al.*	2008	Steel–Ar	CaO·Al_2O_3		10–80	10^{-13}–10^{-15}	[40]
Appelberg *et al.*	2008	Steel–Ar	Ce_2O_3	7100	20		[43]
Kang *et al.*	2011	Steel–Ar	CaO·Al_2O_3			Noncollision	[57]
Wen and Song	2012	Steel–Ar	Ce_2O_2S	6000	<5	Noncollision	[45]
Jiang *et al.*	2014	Steel–Ar	CaO–MgO–Al_2O_3–SiO_2		5		[56]
Mu *et al.*	2017 2018	Steel–Ar	TiN	5430			[50,53]
Tian *et al.*	2018	Steel–Ar	TiN	5430	10		[58]
Mu and Xuan	2019	Steel–Ar	TiO_x–Al_2O_3		10–20		[59]
Wang and Liu	2020	Steel–Ar	Al_2O_3	3900	15–30	10^{-15}–3.0×10^{-14}	[44]
			Ce–Al–O		10–30	1.3×10^{-16}– 2.0×10^{-14}	[44]
			Ce_2O_3	7100	10–30	1.3×10^{-16}– 2.0×10^{-14}	[44]
			Ce–O–S		5–20	2.1×10^{-18}– 6.0×10^{-16}	[44]
Wu *et al.*	2023	Steel–Ar	MgO	3580	5–20	10^{-17}–10^{-15}	[20,60]
Misra *et al.*	2001	Steel–slag	TiN	5430	5		[25]
Lee *et al.*	2001	Steel–slag	Al_2O_3	3900			[41]
Coletti *et al.*	2003	Steel–slag	CaO·Al_2O_3		3–4		[42]
Vantilt *et al.*	2004	Steel–slag	Al_2O_3–MnO–SiO_2			Noncollision	[51]
Wikstrom *et al.*	2008	Steel–slag	CaO·Al_2O_3				[39–40]
Mu *et al.*	2016	Steel–slag	MgO	3580	6	Noncollision	[61]
Misra *et al.*	2000	Steel–slag	Al_2O_3	3900	5	10^{-16}–3.0×10^{-15}	[62]
Michelic *et al.*	2015	Steel–slag	Al_2O_3, Al_2O_3–MgO	3900		Noncollision	[63]

MgO, and SiO_2, and the slags used were mostly liquid Al_2O_3–SiO_2–CaO and Al_2O_3–SiO_2–CaO–MgO. Slag compositions reported in literature are plotted in the Al_2O_3–CaO–SiO_2 diagram shown in Fig. 6 [7,32,41,66–79]. The dissolution mechanisms of different inclusions in the slag are summarized, including diffusion in liquid slag (DLS), boundary layer diffusion (BLD), chemical reaction (CR), and product layer diffusion (PLD) controls. The dissolution mechanism of inclusions in slag was determined by comparing the observed and calculated dissolution curves. The effects of temperature, inclusion properties, and slag composition on inclusion dissolution rates in slag were investigated using CSLM, as summarized in Table 2 [7,32,41,66–90].

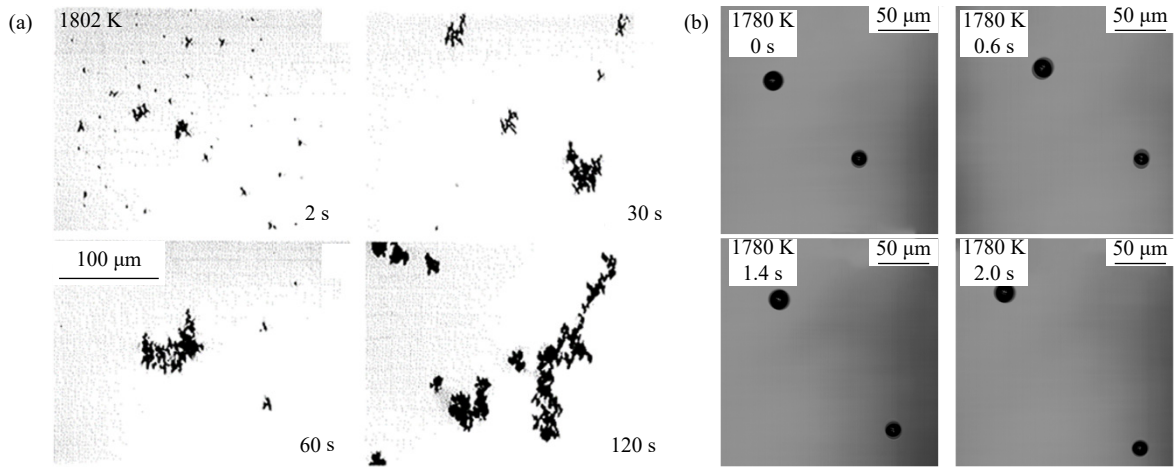

Fig. 2. Collision of inclusions on the surface of the molten steel: (a) solid inclusions [28]; (b) liquid inclusions [60]. (a) Reprinted with permission from Ref. [28]. © 1997 The Iron and Steel Institute of Japan. (b) Reprinted by permission from Springer Nature: *Metall. Mater. Trans. B*, *In-situ* Observation of collision and agglomeration of La_2O_3–La_2S_3 inclusions on surface of molten 304 stainless steels, M.H. Wu, Y. Ren, and L.F. Zhang, Copyright 2024.

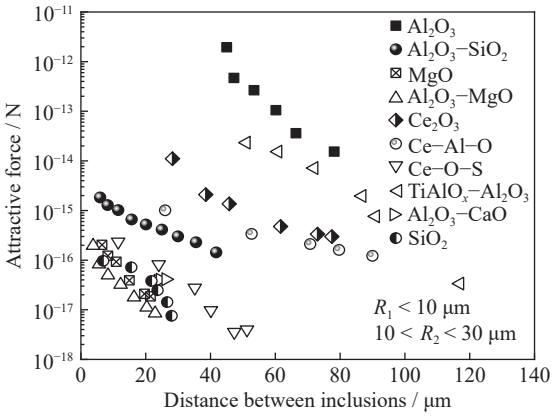

Fig. 3. Change in the attractive force between two inclusions with distance [28,36–38,44,46,52].

Chemical compositions of the inclusions and slag influence the dissolution rates of inclusion particles in slags, as shown in Fig. 7. Fig. 7(a) [90] shows the plots of the inclusion size and dissolution rate. The dissolution rate of inclusions increased with an increase in their diameter. When the experimental temperature was 1773 K, the order of inclusion dissolution rate was $SiO_2 > Al_2O_3 > ZrO_2$. Fig. 7(b) [7,89] and (c) [80] shows the effects of the CaO/Al_2O_3 and CaO/SiO_2 mass ratios of the slag on the dissolution rate of inclusions, respectively. Increasing the CaO/Al_2O_3 and CaO/SiO_2 mass ratios in the slag is beneficial for the dissolution of inclusions in liquid slag. Solid phase formation in slag should be prevented to improve inclusion dissolution. When the temperature increased from 1773 to 1853 K, the dissolution rate of the inclusions increased.

Inclusion dissolution rate was related to the ratio of inclusion solubility to slag viscosity ($\Delta C/\eta$). The correlation between dissolution time of inclusions [7,32,66–67,76,80–81,89] and the parameter $\Delta C/\eta$ is substituted in Eq. (1) [90], as shown in Fig. 8(a). The larger the value of $\Delta C/\eta$, the faster the dissolution of inclusions. However, $\Delta C/\eta$ is a parameter with dimensions, which cannot be used to explain the relationship between dissolution rate and inclusion size. Zhang and Ren [91] proposed the inclusion capacity of refining slag (*Zh*), which is a dimensionless number, as defined in Eq. (2). The dimensionless dissolution rate of inclusions in the slag is proposed in Eq. (3). The empirical equations of *Zh* and *Ry* for the Al_2O_3, ZrO_2, and SiO_2 inclusions were plotted using Eqs. (4)–(6)] [90], as shown in Fig. 8(b). The inclusion capacity of the slag was introduced to predict the dissolution rate of inclusions. The larger the *Zh* number and inclusion size, the longer the dissolution time of the inclusions in liquid slag.

$$\tau = 5.03\times10^{3}\left(\frac{\Delta C}{\eta}\right)^{-1} \tag{1}$$

$$Zh = \frac{g\cdot\rho_{slag}^{2}\cdot(C_{saturation}-C)\cdot d_{p,0}^{3}}{\eta_{slag}^{2}} \tag{2}$$

$$Ry = \frac{1}{v_{slag}\cdot d_{p,0}}\varphi = \frac{\rho_{slag}}{\eta_{slag}\cdot d_{p,0}}\varphi \tag{3}$$

$$Ry_{Al_2O_3} = 2.93\times10^{-6}Zh^{0.165} \tag{4}$$

$$Ry_{ZrO_2} = 1.02\times10^{-6}Zh^{0.089} \tag{5}$$

$$Ry_{SiO_2} = 1.08\times10^{-4}Zh^{0.079} \tag{6}$$

where C is the content of inclusions in the slag; $C_{saturation}$ is the saturation content of inclusions; $d_{p,0}$ is the initial inclusion diameter (m); ρ_{slag} is the slag density (kg/m^3); η_{slag} is the slag dynamic viscosity (kg/(m·s)); g is the gravitational acceleration rate (m/s^2); and φ is the dissolution rate of the inclusion particles in the slag (m^3/s). The *Zh* number represents the dissolution capacity of inclusions by the refining slag; The *Ry* number represents the dissolution rate of inclusion particles in the refining slag.

4. *In-situ* observation of the modification of inclusions in steel

Alloy addition is an effective method to modify inclusions in steel. To address the limitation of sample loading in CSLM, researchers have attempted to observe inclusion

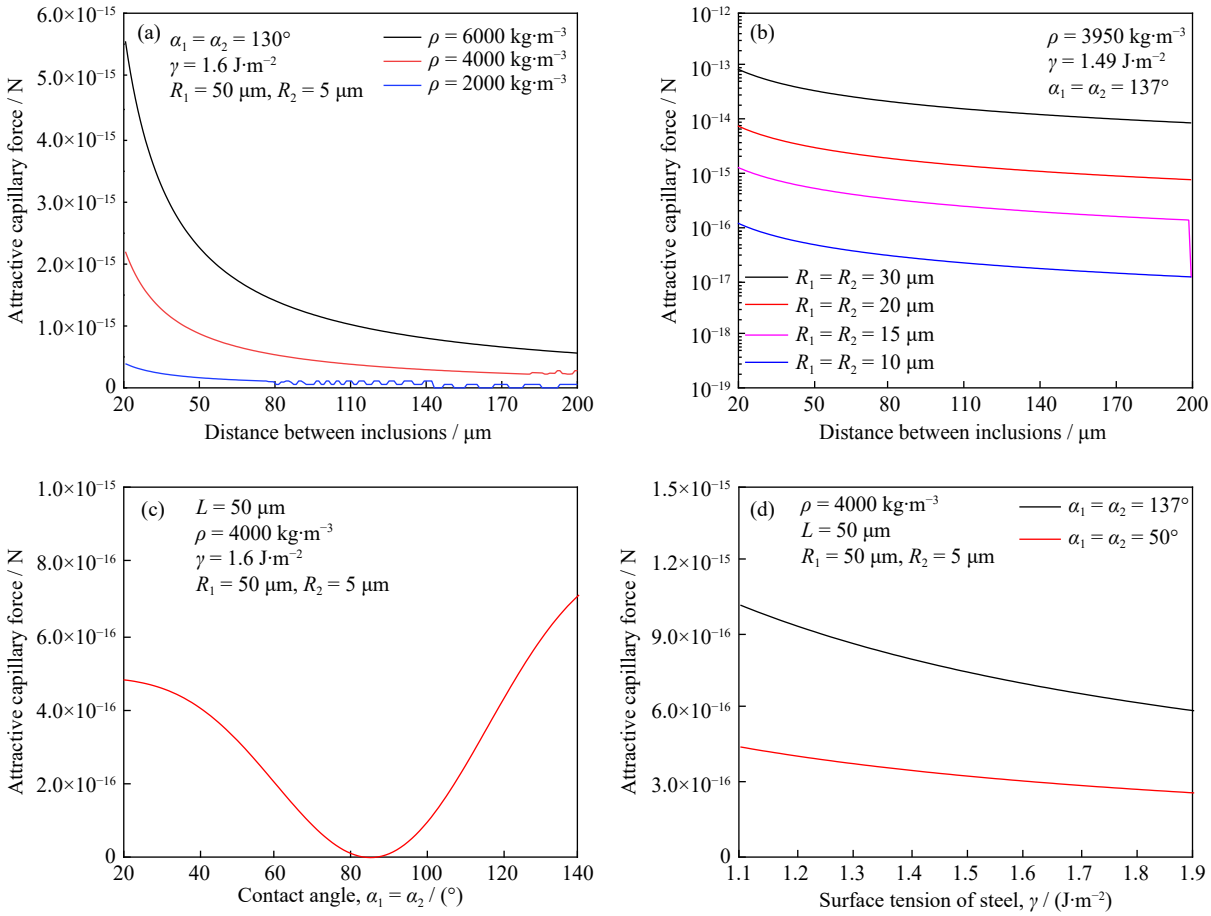

Fig. 4. Calculated attractive force between different inclusions under various conditions: (a) density; (b) size; (c) contact angle [53]; (d) surface tension [53]. (c, d) Adapted from [53]. ρ—Density; α_1, α_2—Contact angle; γ—Surface tension; R_1, R_2—Radius.

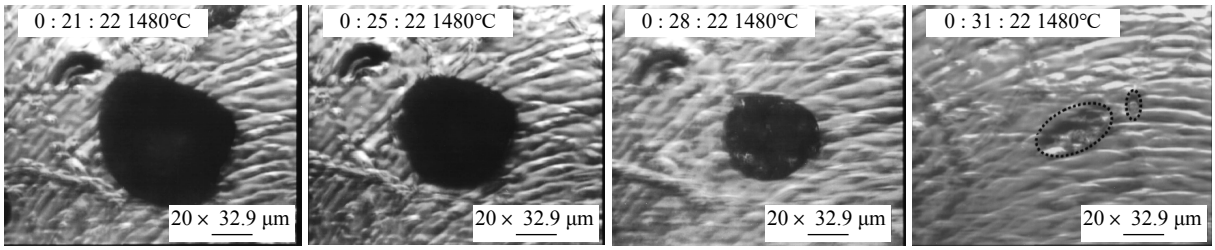

Fig. 5. Images of dissolution process of Al_2O_3 inclusions in slag [32]. Reprinted by permission from Springer Nature: *Metall. Mater. Trans. B*, Kinetics of Al_2O_3 dissolution in CaO–MgO–SiO_2–Al_2O_3 slags: *In Situ* observations and analysis, S. Sridhar and A.W. Cramb, Copyright 2000.

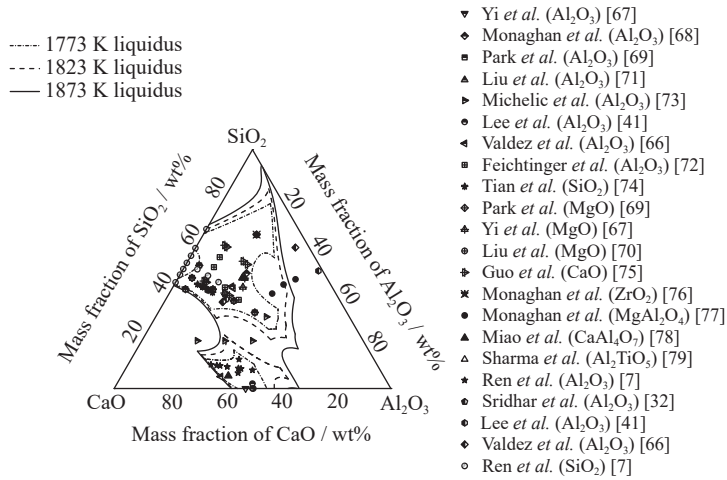

Fig. 6. Reported studies on the inclusion dissolution in CaO–Al_2O_3–SiO_2 slags using CSLM [7,32,41,66–79].

Table 2. Summarized studies on the inclusion dissolution in slags using CSLM [7,32,41,66–90]

Authors	Year	Inclusion	Diameter / μm	Slag system	T / K	Rate-limiting step
Sridhar and Cramb [32]	2000	Al_2O_3	84–138	CASM	1703–1823	BLD
Lee *et al.* [41]	2001	Al_2O_3	50–90	CAS	1723–1773	
Valdez *et al.* [66]	2002	Al_2O_3	200	CAS and CASM	1723–1803	CR and BLD
Yi *et al.* [67]	2003	MgO	190–330	CAM	1723–1873	CR
		Al_2O_3	200			DLS
Fox *et al.* [81]	2004	Al_2O_3		CASM	1523–1773	CR
		ZrO_2	200, 550			
		MgO	200			
		$MgAl_2O_4$				
Monaghan *et al.* [68,76,82]	2004	$MgAl_2O_4$	80	CAS	1750–1805	DLS
	2005	Al_2O_3	100		1777–1850	DLS
		$MgAl_2O_4$	80		1753–1805	DLS
		ZrO_2	100		1750–1805	
Monaghan and Chen [77]	2006	$MgAl_2O_4$	28–35	CAS	1777	DLS
Park *et al.* [69]	2006	MgO		CAS	1823	PLD
Liu *et al.* [71]	2007	Al_2O_3	500	CAS	1743–1903	DLS
Liu *et al.* [70]	2007	MgO	300–400	CASM	1500–1600	BLD
Verhaeghe *et al.* [83]	2007	Al_2O_3	500	CAS	1743	DLS
Park *et al.* [84]	2010	SiC	612, 820	CSM (MnO)	1873	
Sun *et al.* [85]	2013	CaO	400–500	CAS and CASM	1723–1873	
Feichtinger *et al.* [72]	2014	SiO_2	612–696	CAS	1723	DLS
Guo *et al.* [75]	2014	CaO		CAS, CASM	1723–1873	CR, BLD, PLD
Michelic *et al.* [73]	2016	Al_2O_3	400	CASM	1873	DLS
Miao *et al.* [78]	2018	CA_2	222–270	CAS	1773–1873	DLS
Sharma *et al.* [79]	2018	Al_2O_3	320	CAS	1823	BLD
		Al_2TiO_5	400, 900			BLD
Tian *et al.* [74]	2019	SiO_2	~1000	CASM	1743–1803	DLS
Lee *et al.* [86]	2019	MgO	370	MgF_2–CaF_2–LiF, MgF_2–CaF_2–NaF	1473	BLD
Sharma and Dogan [87]	2020	Al_2TiO_5		CAS	1773	BLD
Park *et al.* [88]	2020	Al_2O_3		CASM	1823	DLS
Ren *et al.* [7,89]	2021	Al_2O_3	~200, ~400	CAS	1773–1853	DLS
Ren *et al.* [80]	2022	SiO_2	~200	CASM	1793–1853	DLS
Gou *et al.* [90]	2023	Al_2O_3	100–1100	CAS	1773	DLS
		ZrO_2	500–1100			BLD
		SiO_2	200–900			DLS

Note: Legend of slag system, A—Al_2O_3; S—SiO_2; C—CaO; M—MgO; L—Li_2O.

modifications using CSLM, as shown in Fig. 9. Fig. 9(a) [33] and (b) [92] shows endogenous inclusions colliding with each other on the surface of molten steel, which made tracking the modification behavior of a specific inclusion in steel challenging. Additionally, determining the starting time for inclusion modification was difficult. Thus, extraneous Al_2O_3 particles were proposed to be placed on the surface of the steel sample. After melting the steel sample, the inclusions were modified by the active elements in the steel, as shown in Fig. 9(c) [93]. The melting time of the steel samples was recorded as the start time of the modification reaction. The morphological and compositional evolution of the inclusions during the modification process was analyzed using a combination of CSLM and SEM–EDS. Thus, the method illustrated in Fig. 9(c) was suggested to improve the tracking of modification behavior of a specific inclusion.

Khurana *et al.* [33] placed CaO powder at the bottom of an Al-killed steel sample using the method shown in Fig. 9(a). After melting the steel samples, inclusions in steel before calcium treatment were Al_2O_3. After calcium treatment with CaO powder, the inclusions were modified to Al_2O_3–CaO–CaS. Wang and Liu [92] used the method shown in Fig. 9(b) to heat and melt an Al-killed steel sample, enabling numerous cluster inclusions to float to the surface of the sample. The upper surface of Al-killed steel was cut and placed on top of the Ca-treated steel to expose the aggregated inclusions in the steel for observation. The irregular solid Al_2O_3 inclusions in the steel changed to liquid spherical inclusions within approximately 40 s of the steel melting, as shown in Fig. 10 [92]. Chen *et al.* [93] placed Al_2O_3 particles on the surface of steel samples. Compositional evolution of Al_2O_3 inclusions with different initial sizes during the modification process is shown in Fig. 11 [93]. C3A, C12A7, CA, CA2, CA6, and Al_2O_3 in the right vertical axis represent

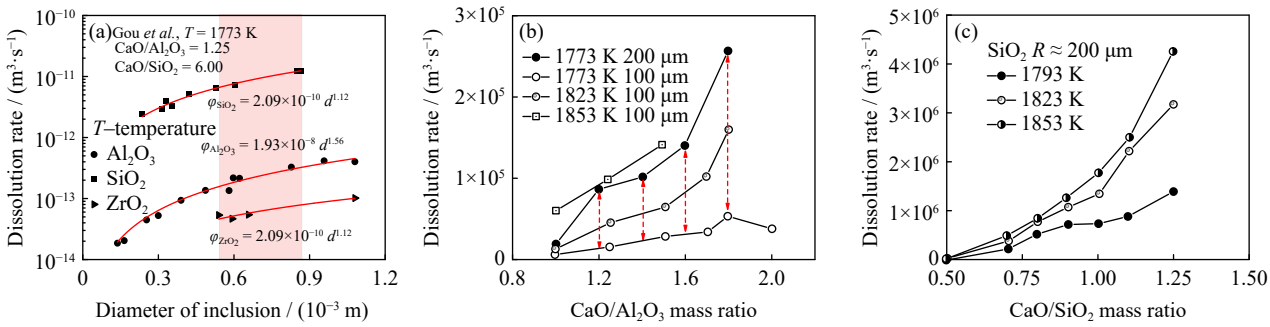

Fig. 7. Influencing factors on the dissolution of inclusion in slag: (a) inclusion diameters [90]; (b) CaO/Al_2O_3 ratio of the slag [7,89]: (c) CaO/SiO_2 ratio of the slag [80]. (a) Reprinted by permission from Springer Nature: *Metall. Mater. Trans. B*, Concept of inclusion capacity of slag and its application on the dissolution of Al_2O_3, ZrO_2 and SiO_2 inclusions in $CaO–Al_2O_3–SiO_2$ slag, L. Gou, H. Liu, Y. Ren, and L. Zhang, Copyright 2023. (b) Reprinted by permission from Springer Nature: *Metall. Mater. Trans. B*, *In situ* observation of the dissolution of Al_2O_3 particles in $CaO–Al_2O_3–SiO_2$ slags, C.Y. Ren, L.F. Zhang, J. Zhang, *et al.*, Copyright 2021; reprinted by permission from Springer Nature: *Int. J. Miner. Metall. Mater*, *In situ* observation of the dissolution kinetics of Al_2O_3 particles in $CaO–Al_2O_3–SiO_2$ slags using laser confocal scanning microscopy, C.Y. Ren, C.D. Huang, L.F. Zhang, *et al.*, Copyright 2023. (c) Reprinted by permission from Springer Nature: *Metall. Mater. Trans. B*, Dissolution of SiO_2 inclusions in $CaO–SiO_2$-based slags *in situ* observed using high-temperature confocal scanning laser microscopy, Y. Ren, P. Zhu, C.Y. Ren, *et al.*, Copyright 2022. φ_{SiO2}, φ_{Al2O3}, and φ_{ZrO2} are dissolution rates of SiO_2, Al_2O_3, and ZrO_2 inclusions, and R is radius.

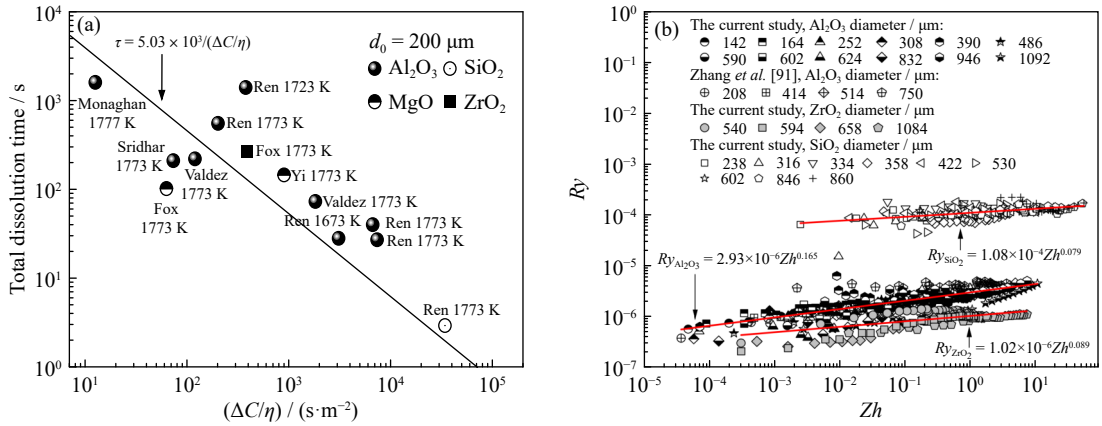

Fig. 8. Reported models for the dissolution rate of inclusions in slags: (a) correlation between dissolution time and $\Delta C/\eta$ of slag [7,32,66–67,76,80–81,89–90]; (b) dependence of the *Ry* number on the *Zh* number [90–91]. (b) Reprinted by permission from Springer Nature: *Metall. Mater. Trans. B*, Concept of inclusion capacity of slag and its application on the dissolution of Al_2O_3, ZrO_2 and SiO_2 inclusions in $CaO–Al_2O_3–SiO_2$ slag, L. Gou, H. Liu, Y. Ren, *et al.*, Copyright 2023. τ—Dissolution time of inclusions.

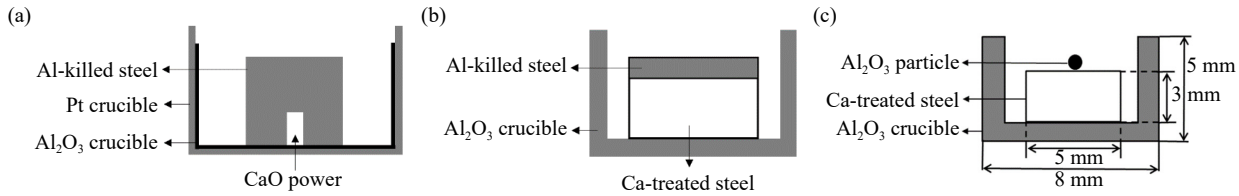

Fig. 9. Schematic of the observation method of the inclusion modification using CSLM: (a) Khurana *et al.* [33]; (b) Wang and Liu [92]; (c) Chen *et al.* [93]. (b) Adapted from Ref. [92]. (c) Reprinted with permission from Ref. [93]. © 2024 The Iron and Steel Institute of Japan.

$3CaO·Al_2O_3$, $12CaO·7Al_2O_3$, $CaO·Al_2O_3$, $CaO·2Al_2O_3$, $CaO·6Al_2O_3$, and Al_2O_3, respectively, which correspond to the mass fraction of CaO in $CaO–Al_2O_3$ inclusions in the left vertical axis. The CaO content in the inclusions gradually increased, and the Al_2O_3 inclusions were gradually modified to $CaO–Al_2O_3$. The modification rates of inclusions decreased with time. The modification rates of the inclusions of various sizes differed owing to the different reaction areas. The liquid fraction of the inclusions gradually increased owing to the increase in CaO content in the inclusions during the modification process.

5. *In-situ* observation of the precipitation and transformation of inclusions in steel

In 1998, Yuki *et al.* [24] observed the precipitation of MnS inclusions during solidification and cooling processes of an Fe–42wt%Ni alloy using CSLM, as shown in Fig. 12.

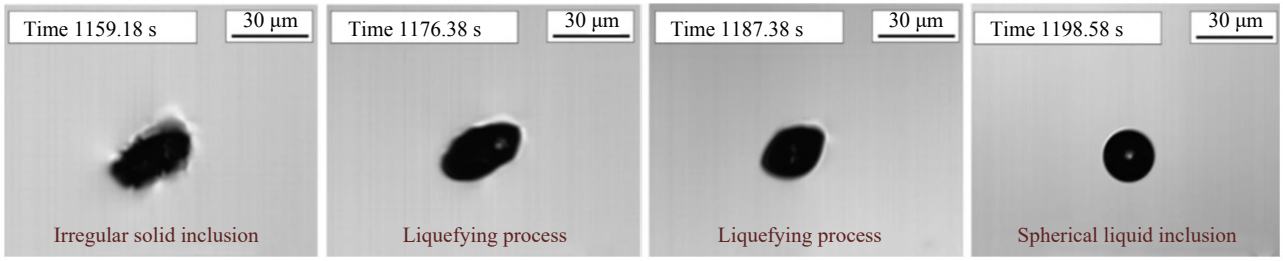

Fig. 10. ***In-situ*** **observation of the modification of an endogenous inclusion using CSLM [92]. Reprinted by permission from Springer Nature:** ***Metall. Mater. Trans. B*****,** ***In situ*** **observation of transient evolution of inclusions by Ca treatment in molten steel, Y.G. Wang and C.J. Liu, Copyright 2022.**

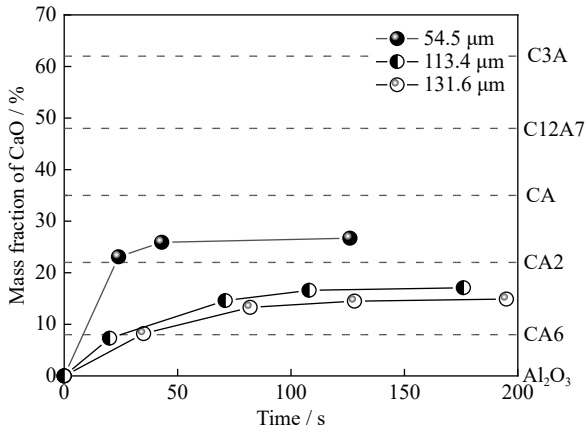

Fig. 11. Composition evolution of Al_2O_3 inclusions with different initial sizes during the modification process analyzed using CSLM and SEM–EDS. Reprinted with permission from Ref. [93]. © 2024 The Iron and Steel Institute of Japan.

Recently, several scholars have utilized CSLM to study the precipitation of inclusions during cooling and heating processes, as summarized in Table 3 [24–25,58,94–113]. The morphology of MnS inclusions has an influence on the properties of steel. Valdez *et al.* [95] observed the precipitation of MnS inclusions during cooling and heating process of steel containing 0.05wt% S. Nakama *et al.* [96] reported that the sulfide precipitation was related to the solidification sequence of Fe–Cr–Ni alloys, which depended on Ni and Cr contents. Both high-Ni, low-Cr alloys solidifying in the primary γ field and low-Ni, high-Cr alloys solidifying in the primary δ field led to sulfide precipitation in the enriched melt ahead of the dendrite fronts. In low-Ni, high-Cr alloys, sulfides are formed via liquid phase separation. By contrast, in intermediate Ni and Cr alloys with limited primary phase-field solidification, sulfides are formed within the solid phase. Several researchers have investigated the correlation between MnS precipitation and the liquid fraction of steel during solidification [97–98,100–101,103,107]. The precipitation of MnS is also related to elemental concentrations in steels. The effects of Cu [114–115] and Te [102] contents on the precipitation characteristics and temperature of MnS were observed using CSLM. The addition of Cu or Te slows precipitation of MnS at the grain boundaries, which is beneficial for the uniform distribution of MnS in the steel. In 2001, Misra *et al.* [25] studied the precipitation of TiN inclusions at the steel–slag interface using CSLM. The morphology of TiN varied with temperature. At a temperature lower than the solidus of steel, increase in temperature increased the rate of TiN inclusions in steel. Tian *et al.* [58] *in-situ* observed the precipitation, collision, and dissolution behaviors of TiN inclusions on the surface of molten GCr15-bearing steel.

In 1996, Chikama *et al.* [27] observed the crystal growth process of Fe–C alloys and found that inclusions in steel were engulfed and entrapped by growing crystals during solidification and cooling of molten steel. Yin *et al.* [30,116] determined the flow direction and velocity of a molten steel surface near the solid–melt interface, as shown in Fig. 13 [116]. The velocity of the solutal Marangoni flow was very high, pushing the inclusions up to the surface along the steel–metal interface. These features were responsible for the entrapment of inclusions and solute segregation during the solidification and cooling of steel. Chen *et al.* [117] reported that the high growth rate of the δ phase promoted the entrapment of inclusions. Yan *et al.* [118] reported that the movement of inclusions at the solidification front can be of three types: attraction, repulsion, and no effect.

CSLM has also been widely used to observe changes in inclusions during solid steel heating. In 2011, Shao *et al.* [108–109,119] utilized CSLM to observe morphological

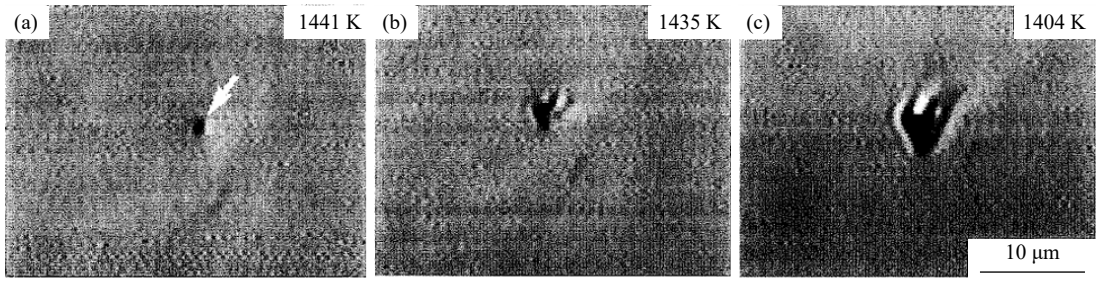

Fig. 12. Precipitation of MnS inclusions in steel observed using CSLM. Reprinted with permission from Ref. [24]. © 1998 The Iron and Steel Institute of Japan.

Table 3. Summarized *in-situ* observation of the precipitation and transformation of inclusions during solidification and heating processes [24–25,58,94–113]

Authors	Year	Steel	Process	Inclusion	Temperature / K
Yuki *et al.* [24]	1998	Fe–Ni alloys	Solidification	MnS	1329–1438
Misra *et al.* [25]	2001	Stainless steel	Solidification	TiN	1553–1593, 1623–1773
Wang *et al.* [94]	2003	Al-killed Ca-treated steel	Solidification	CaS	
Valdez et *al.* [95]	2005	Resulfurized steel	Solidification	MnS	
Nakama *et al.* [96]	2009	Fe–Cr–Ni alloys	Solidification	MnS	1669–1738
Luo *et al.* [97]	2011	49MnVS3 steel	Solidification	MnS	
Hu *et al.* [98]	2018	Sulfur-bearing steel	Solidification	MnS	1700, 1746
Tian *et al.* [58,99]	2018	GCr15-bearing steel	Solidification	TiN	1640–1840
Tanaka *et al.* [100]	2019	High-carbon steel	Solidification	MnS	
Zeng *et al.* [101]	2020	High-sulfur microalloyed steel	Solidification	MnS	1703, 1713
Shen *et al.* [102]	2021	Te-treated resulfurized special steel	Solidification	Mn–S–Te	
Chu *et al.* [103]	2022	Medium/high-manganese steel	Solidification	MnS	
Cao *et al.* [104]	2022	GCr15-bearing steel	Solidification	MgO–TiN	1597
Liu *et al.* [105]	2022	Al-killed Ca-treated steel	Solidification	CaO–MgO–Al_2O_3	1273–1473
Zhu *et al.* [106]	2023	High-titanium steel	Solidification	TiC_xN_{1-x}	1649, 1707
Cao *et al.* [107]	2024	High-Al medium-Mn steel	Solidification	MnS	
Shao *et al.* [108]	2011	Free-cutting steel	Heating	MnS	873–1473
Shao *et al.* [109]	2011	Free-cutting steel	Heating	MnS	1463
Wang *et al.* [110]	2018	EH36 steel	Heating	TiN	1473
Wang *et al.* [111]	2018	EH36 steel	Heating	MnS	1473
Wang *et al.* [112]	2019	High-carbon steel	Heating	Rare-earth inclusions	1473, 1623
Song *et al.* [113]	2023	Heavy rail steel	Heating	MnS, oxides	1323, 1393

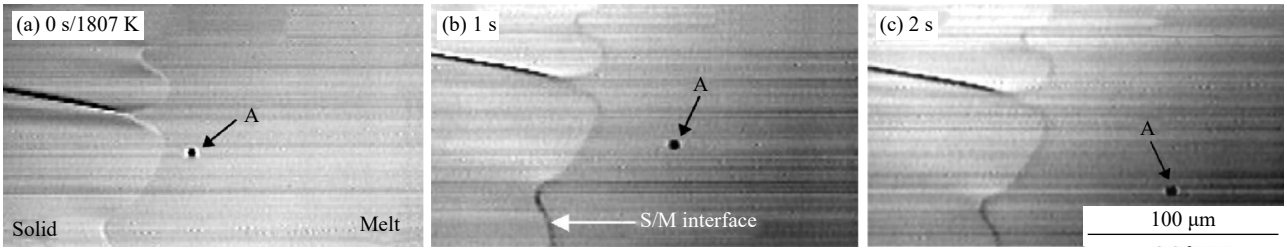

Fig. 13. Movement of an inclusion at the solid–melt interface due to surface flow during steel solidification at a cooling rate of 0.025 K/s [116]. Reprinted by permission from Springer Nature: *Metall. Mater. Trans. B*, Marangoni flow at the gas/melt interface of steel, H.B. Yin and T. Emi, Copyright 2003.

evolution of large slender MnS inclusions in sulfur-containing steels, as shown in Fig. 14 [108]. Moreover, they proposed a mechanism for the evolution of MnS inclusions during heating. The elongated MnS inclusions shrank and fractured during heating, forming spherical MnS. Song *et al.* [113] observed the formation of MnS on oxide inclusions during heating of heavy rail steel. Wang *et al.* [111] reported that the amount of MnS decreased during EH36 steel heating at 1473 K and TiN inclusions precipitated in the steel. Moreover, CSLM can be used to observe the changes in ox-

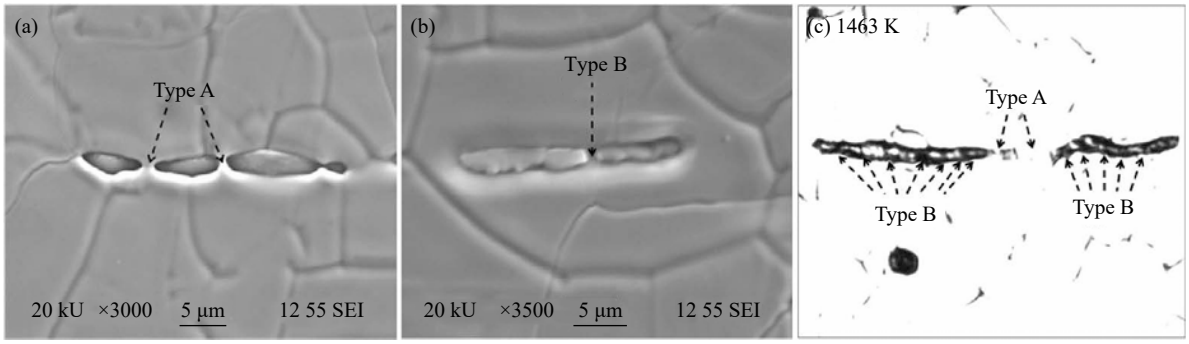

Fig. 14. Observation of the morphological evolution of slender MnS inclusions in free-cutting steel at 1463 K using CSLM [108]. Reprinted with permission from Ref. [108]. © 2011 The Iron and Steel Institute of Japan.

ide inclusions during solid steel heating. Liu *et al.* [105] used CSLM to *in-situ* observe that inclusions evolved from CaO–MgO–Al_2O_3 to CaO–MgO–Al_2O_3–CaS in solid Al-killed Ca-treated steels at 1273–1473 K. High temperatures promoted the formation of CaS in the inclusions owing to the large diffusion rate of the elements. They concluded that MnS precipitation was primarily related to the Mn and S contents and temperature of the steel and the formation of TiN was influenced by the Ti and N contents and temperature of the steel.

6. *In-situ* observation of the formation of intragranular acicular ferrite at inclusions in steel

Oxide metallurgy was invented in the 1990s and has been widely used in manufacturing of high-strength steel components such as ship plates and pipes. During the welding process, high heat input leads to a reduction in toughness. Nano-scale inclusions have been reported to pin the grain boundary. Moreover, micron-scale inclusions can promote the nucleation of AF on the surface of inclusions, which has become an effective method to increase steel toughness at low temperatures [120–125]. Mu *et al.* [126] reviewed the application of CSLM in the observation of AF growth induced by inclusions. The key step in oxide metallurgy is adjusting the elements to form inclusions that induce AF nucleation and to control the microstructure by controlling the cooling rate. The dependence of the inclusion characteristics and temperature parameters on the volume fraction, size, and formation temperature of AF has been widely studied. In 1999, Hanamura *et al.* [31] used CSLM to observe the formation of polygonal and Widmanstätten ferrites on the surfaces of oxides and sulfides. Since then, numerous scholars have conducted experimental studies on the induction of AF nucleation by inclusions using CSLM, as summarized in Table 4 [31,46,127–144].

Table 4. Summarized studies on the induction of AF nucleation by inclusions using CSLM [31,45,127–144]

Author	Year	Inclusions		Heating cycles			Quantitative of ferrite			
		Type	Size / μm	Temperature / K	Holding time / s	Cooling rate / ($K \cdot s^{-1}$)	Fraction / wt%	Formation temperature / °C	Grain size / μm	Kinetics
Hanamura *et al.* [31]	1999	Ti–Si–O	No	1673	1	10	No	737	No	Yes
Terasaki [127]	2007	Al–O	<2.5	1673	1	2	No	No	No	No
Zhang *et al.* [128]	2009	Ti–Al–Mn–O–MnS	No	1673	1–300	5	0–9	650–750	100–400	No
Hu *et al.* [129]	2011	Ti–Al–Mn–Si–O–MnS	1–2	1673	1–600	5	50–90	550–700	132–251	No
Wen and Song [45]	2012	$AlCeO_3$–Ce_2O_2S	1–5	1476	600	5	No	557–623	120	No
Wan *et al.* [130]	2013	Ti–Al–Mn–O–MnS	No	1673	5	5	No	634.4	No	No
Wan *et al.* [131]	2013	Ti–Mn–O–MnS	No	1673	5–30	5	No	840	150	Yes
Mu *et al.* [132]	2014	TiO_x–MnS	>1.2	1823	60	216	10–50	No	245–968	Yes
Jiang *et al.* [133]	2015	Ti–Al–Mn–Si–O–MnS	No	1673	600	5	No	543–638	No	No
Wan *et al.* [134]	2015	Zr–Ti–Al–O	No	1573–1673	5–30	5	No	550–620	46–166	Yes
Wu *et al.* [135]	2015	Al–Ti–Mg–O	0.9–1.1	1523–1673	180–300	5	No	650	22–139	No
Mu *et al.* [136]	2016	Ti–Al–Mn–Si–O–MnS	No	1473–1673	0–600	0.1–1.2	0–80	600–760	100–900	No
Lin *et al.* [137]	2017	Mg–Al–O–MnS	1.4–2.4	1573	180	1–20	7–26	559–729	60–100	No
Loder and Michelic [138]	2017	Ti–Mn–Al–O–MnS	>1.2	1673	100	7	72–85	653–670	125–210	No
Yang *et al.* [139]	2019	Ti–Zr–Al–O–MnS	1.4–1.9	1473	60	0.5–10	26–46	540–691	64.53	Yes
Wang *et al.* [140]	2020	Ti–Ca–Zr–Al–O–MnS	No	1673	180	2–15	75–82	600–680	170–180	Yes
Wang *et al.* [141]	2022	TiN–MnS	1.3–2.7	1763	1	0.2–10	13–83	No	206–704	No
Liu *et al.* [142]	2022	Ca–Al–O–MnS	No	1623	1	12.5	60–77	600–700	100–114	Yes
Yao *et al.* [143]	2022	Al–Ti–Mn–O–MnS	1.2–1.4	1523–1673	300	3	13.4–78.7	667–767	113–293	Yes
Xie *et al.* [144]	2023	No	No	1673	3	0.6–10.5	No	532.3–680.7	No	Yes

Fig. 15(a) [128] shows the nucleation and growth of AF in a steel sample during heating at 1400°C for 200 s using CSLM. The AFs grew along the four directions of the inclusion. Fig. 15(b) [128] shows the hard impingement of the AFs. Nucleation initiated at both the austenite grain boundaries and inclusions. Laths grew from clean austenite grain boundaries as Widmanstätten ferrite, which was inhibited by the growth of intragranular AF. Subsequently, the growths of AF impinged on each other to generate a fine interlocking microstructure. Thus, the growth process of AF primarily includes three steps: primary nucleation on the inclusions, sympathetic nucleation on the broad side of the primary ferrite, and impingement between AFs. Fig. 16 shows the summarized average growth rates of AFs for various oxide inclusions. The growth rate of the AFs induced by various inclusions was in the range of 0.03–33.3 μm/s. At a cooling rate of 3–5 K/s, the order of growth rates of AFs induced by different inclusions, as reported in literature, was Ti–O [126] < Ti–Ca–Zr–Al–O [140] < Mg–O [137] < Ti–Zr–Al–O [139] < Ti–Al–O [143] < Mn–Ti–Al–O [143] < Zr–Ti–Al–O [134]. Notably, the ZrO content in the Zr–Ti–Al–O inclusions was higher than the TiO_x content and the TiO_x content in the Ti–Zr–Al–O inclusions was higher than the ZrO content. The growth rate of the AFs induced by inclusions may also change when the heat-treatment parameters and steel composition are altered.

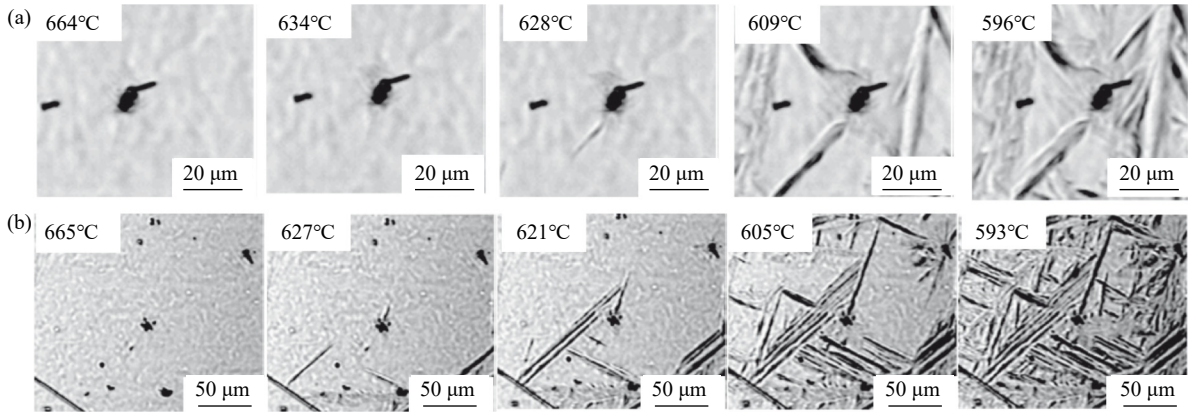

Fig. 15. *In-situ* observation of morphology of AF at inclusions in steel: (a) nucleation and growth of AFs; (b) hard impingements between the AFs [128]. Reprinted from *Acta Mater.*, 58, D. Zhang, H. Terasaki, and Y.I. Komizo, *In situ* observation of the formation of intragranular acicular ferrite at non-metallic inclusions in C–Mn steel, 1369-1378, Copyright 2010, with permission from Elsevier.

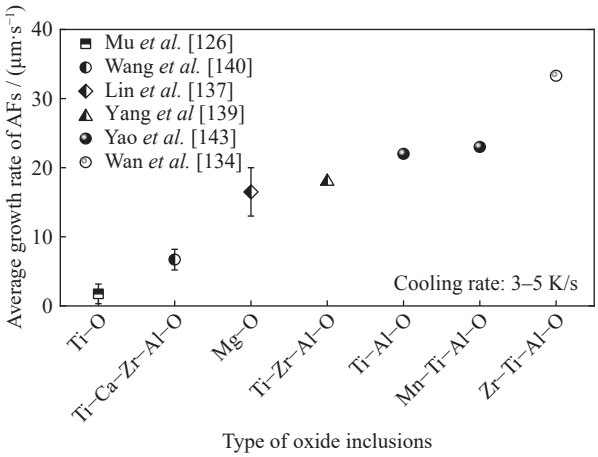

Fig. 16. Summarized average growth rates of AFs for various oxide inclusions.

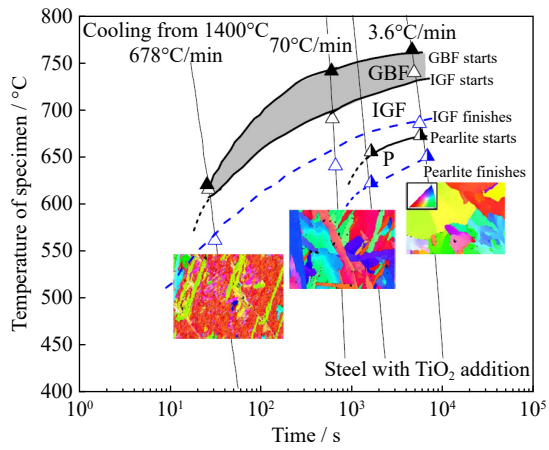

Fig. 17. CCT diagram of the steel with TiO_2 addition, analyzed by CSLM, DSC, and EBSD [126].

As CSLM can be used to measure steel phase transition temperature, a method combining CSLM and differential scanning calorimetry (DSC) was proposed to monitor the final continuous cooling transformation (CCT) diagram, as shown in Fig. 17 [126]. Electron backscatter diffraction (EBSD) micrographs showed that the microstructure became very fine at high cooling rates. The CCT diagram can be used to design heating and cooling parameters in oxide metallurgy.

7. Opportunities and challenges in *in-situ* observation of inclusions using CSLM

The characteristics of inclusions have a significant influence on steel performance [145–152]. The formation, collision, dissolution, modification, and precipitation of inclusions during steel production have been extensively studied using CSLM. However, the following directions will be the focus of future research in *in-situ* observation of inclusions

using CSLM.

(1) Collision of complex inclusions at steel–slag interface. Previous studies have primarily focused on the *in-situ* observation of the collision of pure inclusions at the steel–Ar interface. However, the collisions of complex inclusions have not been extensively studied. Additionally, *in-situ* observation of collision of inclusions at the steel–slag interface owing to the wettability difference between the steel–Ar and steel–slag interfaces is necessary.

(2) Dissolution of complex inclusions in the slag at the steel–slag interface. The dissolution of pure inclusions in liquid slag has been widely observed *in-situ* in a previous study to optimize slag composition. To simulate the process of inclusion dissolution, *in-situ* observation of the dissolution of inclusions in slag at the steel–slag interface is necessary. Furthermore, complex inclusions are formed in steel during steel production. However, the dissolution of complex inclusions in slags has not been extensively studied.

(3) *In-situ* observation of inclusion modifications. Several methods have been proposed for the *in-situ* observation of the modification of inclusions by dissolved elements in steel. However, further investigations are required on not only Ca modification but also modification by other active elements. Moreover, developing an additional technique during the CSLM experiments to improve the understanding of the modification process of inclusions will be useful.

(4) *In-situ* observation of inclusion transformation in steel during solidification and heating processes. The precipitations of MnS and TiN have been extensively studied. The effects of temperature and steel composition on the precipitation of inclusions have been elucidated. Recently, transformation of inclusions during solidification and heating processes has been reported. However, *in-situ* observations of the transformation of oxide inclusions in steel during solidification and heating processes have rarely been reported.

(5) Quantitative correlation between AF formation and inclusion characteristics. The effects of temperature and grain size on AF formation and growth have been widely studied. The formation and growth of AF were influenced not only by the heating and cooling parameters but also by the size and composition of inclusions. Thus, comprehensive experiments are necessary to investigate the quantitative relationship between AF formation and inclusion characteristics.

8. Conclusions

(1) The collisions of various inclusions observed *in-situ* using CSLM are summarized. The solid inclusions exhibited a significant attractive force, with a high tendency to collide. However, pure liquid inclusions rarely collided because of their low attraction. The order of capillary forces for different inclusions was Al_2O_3 > $TiAlO_x$–Al_2O_3 > Ce_2O_3 > Ce–Al–O > Al_2O_3–SiO_2 > Ce–O–S > Al_2O_3–CaO > SiO_2 > MgO > $MgAl_2O_4$. In future studies, collisions of complex inclusions should be investigated as these inclusions are actually formed in molten steel.

(2) Increasing the CaO/Al_2O_3 and CaO/SiO_2 ratios is beneficial for the dissolution of inclusions in liquid slag. Solid phase formation in the slag should be prevented to improve inclusion dissolution. The reported models are summarized to predict the dissolution rate of the inclusions in the slag. To simulate the process of inclusion dissolution, *in-situ* observation of the dissolution of inclusions in the slag at the steel–slag interface is necessary.

(3) Several methods have been proposed for *in-situ* observation of inclusion modification by dissolved elements in steel. The morphological and compositional evolution of the inclusions during the reaction process were observed *in-situ* using a combination of CSLM and SEM–EDS. Developing an additional technique during CSLM experiments to further reveal the modification process of the inclusions will be useful.

(4) *In-situ* observation of MnS and TiN precipitation has been widely studied, whereas the *in-situ* observation of the transformation of oxide inclusions in steel during solidification and heating processes has rarely been reported.

(5) CSLM can be used to observe phase transition temperature induced by inclusions on a sample surface. The effects of temperature and inclusion characteristics on AF formation have been widely studied. At a cooling rate of 3–5 K/s, the order of growth rates of AFs induced by different inclusions, as reported in literature, was Ti–O < Ti–Ca–Zr–Al–O < Mg–O < Ti–Zr–Al–O < Mn–Ti–Al–O < Ti–Al–O < Zr–Ti–Al–O. Further experiments are necessary to investigate the quantitative relationship between AF formation and inclusion characteristics.

Acknowledgements

This work was financially supported by the National Key R&D Program (No. 2023YFB3709900), the National Nature Science Foundation of China (No. U22A20171), China Baowu Low Carbon Metallurgy Innovation Foundation (No. BWLCF202315), the High Steel Center (HSC) at North China University of Technology and University of Science and Technology Beijing, China.

Conflict of Interest

Ying Ren and Lifeng Zhang are editorial board members for this journal and were not involved in the editorial review or the decision to publish this article. The authors have no relevant financial or non-financial interests to disclose.

References

[1] Y. Kang, M. Thunman, S.C. Du, T. Morohoshi, K. Mizukami, and K. Morita, Aluminum deoxidation equilibrium of molten iron–aluminum alloy with wide aluminum composition range at 1 873 K, *ISIJ Int.*, 49(2009), No. 10, p. 1483.

[2] M.K. Paek, J.M. Jang, Y.B. Kang, and J.J. Pak, Aluminum deoxidation equilibria in liquid iron: Part I. experimental, *Metall. Mater. Trans. B*, 46(2015), No. 4, p. 1826.

[3] M. Paek, J. Pak, and Y. Kang, Aluminum deoxidation equilib-

ria in liquid iron: Part II. Thermodynamic modeling, *Metall. Mater. Trans. B*, 46(2015), p. 2224.

[4] H.J. Duan, Y. Ren, B.G. Thomas, and L.F. Zhang, Agglomeration of solid inclusions in molten steel, *Metall. Mater. Trans. B*, 50(2019), No. 1, p. 36.

[5] H.J. Duan, Y. Ren, and L.F. Zhang, Effects of interphase forces on fluid flow in gas-stirred steel ladles using the eulerian–Lagrangian multiphase approach, *JOM*, 70(2018), No. 10, p. 2128.

[6] H.J. Duan, Y. Ren, and L.F. Zhang, Modeling of turbulent flow around bubbles in molten steel, *Steel Res. Int.*, 90(2019), No. 6, art. No. 1800576.

[7] C.Y. Ren, L.F. Zhang, J. Zhang, S.J. Wu, P. Zhu, and Y. Ren, *In situ* observation of the dissolution of Al_2O_3 particles in CaO–Al_2O_3–SiO_2 slags, *Metall. Mater. Trans. B*, 52(2021), No. 5, p. 3288.

[8] Y.D. Gu, Y. Ren, and L.F. Zhang, *In-situ* observation on dissolution of CaO–SiO_2–Al_2O_3 complex inclusions in refining slag, *J. Iron Steel Res. Int.*, 32(2025), p. 376.

[9] M. Valdez, G.S. Shannon, and S. Sridhar, The ability of slags to absorb solid oxide inclusions, *ISIJ Int.*, 46(2006), No. 3, p. 450.

[10] N. Verma, P. Pistorius, R. Fruehan, M. Potter, M. Lind, and S. Story, Transient Inclusion evolution during modification of alumina inclusions by calcium in liquid steel: Part II. Results and discussion, *Metall. Mater. Trans. B*, 42(2011), p. 720.

[11] N. Verma, P.C. Pistorius, R.J. Fruehan, M. Potter, M. Lind, and S. Story, Transient inclusion evolution during modification of alumina inclusions by calcium in liquid steel: Part I. background, experimental techniques and analysis methods, *Metall. Mater. Trans. B*, 42(2011), No. 4, p. 711.

[12] N. Verma, P.C. Pistorius, R.J. Fruehan, M.S. Potter, H.G. Oltmann, and E.B. Pretorius, Calcium modification of spinel inclusions in aluminum-killed steel: Reaction steps, *Metall. Mater. Trans. B*, 43(2012), No. 4, p. 830.

[13] Y. Ren, L.F. Zhang, and S.S. Li, Transient evolution of inclusions during calcium modification in linepipe steels, *ISIJ Int.*, 54(2014), No. 12, p. 2772.

[14] P.C. Yan, S.G. Huang, L. Pandelaers, J. Van Dyck, M.X. Guo, and B. Blanpain, Effect of the CaO–Al_2O_3-based top slag on the cleanliness of stainless steel during secondary metallurgy, *Metall. Mater. Trans. B*, 44(2013), No. 5, p. 1105.

[15] Y. Ren, L.F. Zhang, W. Fang, S.J. Shao, J. Yang, and W.D. Mao, Effect of slag composition on inclusions in Si-deoxidized 18Cr–8Ni stainless steels, *Metall. Mater. Trans. B*, 47(2016), No. 2, p. 1024.

[16] Y. Ren and L.F. Zhang, Thermodynamic model for prediction of slag–steel–inclusion reactions of 304 stainless steels, *ISIJ Int.*, 57(2017), No. 1, p. 68.

[17] B. Coletti, B. Gommers, C. Vercruyssen, B. Blanpain, P. Wollants, and F. Haers, Reoxidation during ladle treatment, *Ironmaking Steelmaking*, 30(2003), No. 2, p. 101.

[18] H. Goto and K.I. Miyazawa, Reoxidation behavior of molten steel in non-killed and Al-killed steels, *ISIJ Int.*, 38(1998), No. 3, p. 256.

[19] Y. Higuchi, Y. Tago, S. Fukagawa, T. Kanai, and A. Mutoh, Reoxidation behavior in Al killed steel during casting, *Tetsu-to-Hagane*, 85(1999), No. 5, p. 375.

[20] M.H. Wu, C.Y. Ren, Y. Ren, and L.F. Zhang, *In situ* observation of the agglomeration of MgO–Al_2O_3 inclusions on the surface of a molten GCr15-bearing steel, *Metall. Mater. Trans. B*, 54(2023), No. 3, p. 1159.

[21] S.F. Yu, Y. Lei, M.L. Xie, A.G. Huang, and Z.Y. Li, Nucleation mechanisms of intragranular ferrite (IGF), *J. Iron Steel Res.*, 17(2005), No. 1, p. 47.

[22] Y. Arai, T. Emi, H. Fredriksson, and H. Shibata, *In-situ* observed dynamics of peritectic solidification and δ/γ transformation of Fe–3 to 5 At. pct Ni alloys, *Metall. Mater. Trans. A*, 36(2005), No. 11, p. 3065.

[23] H. Shibata, Y. Arai, M. Suzuki, and T. Emi, Kinetics of peritectic reaction and transformation in Fe–C alloys, *Metall. Mater. Trans. B*, 31(2000), No. 5, p. 981.

[24] N. Yuki, H. Shibata, and T. Emi, Solubility of MnS in Fe-Ni alloys as determined by *in situ* observation of precipitation of MnS with a confocal scanning laser microscope, *ISIJ Int.*, 38(1998), No. 4, p. 317.

[25] P. Misra, S. Sridhar, and A.W. Cramb, *In-situ* observation of TiN precipitates at stainless steel/CaO–Al_2O_3–MgO–SiO_2 interface, *Metall. Mater. Trans. B*, 32(2001), No. 5, p. 963.

[26] M. Minsky, Memoir on inventing the confocal scanning microscope, *Scanning*, 10(1988), No. 4, p. 128.

[27] H. Chikama, H. Shibata, T. Emi, and M. Suzuki, "*In-situ*" real time observation of planar to cellular and cellular to dendritic transition of crystals growing in Fe–C alloy melts, *Mater. Trans. JIM*, 37(1996), No. 4, p. 620.

[28] H.B. Yin, H. Shibata, T. Emi, and M. Suzuki, "*In-situ*" observation of collision, agglomeration and cluster formation of alumina inclusion particles on steel melts, *ISIJ Int.*, 37(1997), No. 10, p. 936.

[29] H. Shibata, H. Yin, and T. Emi, The capillary effect promoting collision and agglomeration of inclusion particles at the inert gas–steel interface, *Philos. Trans. R. Soc. Lond. Ser. A: Math. Phys. Eng. Sci.*, 356(1998), No. 1739, p. 957.

[30] H. Shibata, H.B. Yin, S. Yoshinaga, T. Emi, and M. Suzuki, *In-situ* observation of engulfment and pushing of nonmetallic inclusions in steel melt by advancing melt/solid interface, *ISIJ Int.*, 38(1998), No. 2, p. 149.

[31] T. Hanamura, H. Shibata, Y. Waseda, *et al.*, *In-situ* observation of intragranular ferrite nucleation at oxide particles, *ISIJ Int.*, 39(1999), No. 11, p. 1188.

[32] S. Sridhar and A.W. Cramb, Kinetics of Al_2O_3 dissolution in CaO–MgO–SiO_2–Al_2O_3 slags: *in situ* observations and analysis, *Metall. Mater. Trans. B*, 31(2000), No. 2, p. 406.

[33] B. Khurana, S. Spooner, M.B.V. Rao, G.G. Roy, and P. Srirangam, *In situ* observation of calcium oxide treatment of inclusions in molten steel by confocal microscopy, *Metall. Mater. Trans. B*, 48(2017), No. 3, p. 1409.

[34] H.B. Yin, H. Shibata, T. Emi, and M. Suzuki, Characteristics of agglomeration of various inclusion particles on molten steel surface, *ISIJ Int.*, 37(1997), No. 10, p. 946.

[35] G.F. Liang, C.Q. Wang, and Y. Fang, *In situ* observation on movement and agglomeration of inclusion in solidliquid mush zone during melting of stainless steel aisi304, *Acta Metall. Sin.*, 42(2006), No. 7, p. 708.

[36] S. Kimura, K. Nakajima, and S. Mizoguchi, Behavior of alumina-magnesia complex inclusions and magnesia inclusions on the surface of molten low-carbon steels, *Metall. Mater. Trans. B*, 32(2001), No. 1, p. 79.

[37] S. Kimura, Y. Nabeshima, K. Nakajima, and S. Mizoguchi, Behavior of nonmetallic inclusions in front of the solid-liquid interface in low-carbon steels, *Metall. Mater. Trans. B*, 31(2000), No. 5, p. 1013.

[38] K. Nakajima and S. Mizoguchi, Capillary interaction between inclusion particles on the 16Cr stainless steel melt surface, *Metall. Mater. Trans. B*, 32(2001), No. 4, p. 629.

[39] J. Wikström, K. Nakajima, H. Shibata, A. Tilliander, and P. Jönsson, *In situ* studies of the agglomeration phenomena for calcium–alumina inclusions at liquid steel–liquid slag interface and in the slag, *Mater. Sci. Eng. A*, 495(2008), No. 1-2, p. 316.

[40] J.Wikström, K.Nakajima, H.Shibata, A.Tilliander, and P.Jönsson, *In situ* studies of agglomeration between Al_2O_3–CaO inclusions at metal/gas, metal/slag interfaces and in slag, *Ironmaking Steelmaking*, 35(2008), No. 8, p. 589.
[41] S.H. Lee, C. Tse, K.W. Yi, *et al*., Separation and dissolution of Al_2O_3 inclusions at slag/metal interfaces, *J. Non Cryst. Solids*, 282(2001), No. 1, p. 41.
[42] B. Coletti, B. Blanpain, S. Vantilt, and S. Sridhar, Observation of calcium aluminate inclusions at interfaces between Ca-treated, Al-killed steels and slags, *Metall. Mater. Trans. B*, 34(2003), No. 5, p. 533.
[43] J. Appelberg, K. Nakajima, H. Shibata, A. Tilliander, and P. Jönsson, *In situ* studies of misch-metal particle behavior on a molten stainless steel surface, *Mater. Sci. Eng. A*, 495(2008), No. 1-2, p. 330.
[44] Y.G. Wang and C.J. Liu, Agglomeration characteristics of various inclusions in Al-killed molten steel containing rare earth element, *Metall. Mater. Trans. B*, 51(2020), No. 6, p. 2585.
[45] B. Wen and B. Song, *In situ* observation of the evolution of intragranular acicular ferrite at Ce-containing inclusions in 16Mn steel, *Steel Res. Int.*, 83(2012), No. 5, p. 487.
[46] Y.G. Wang and C.J. Liu, Agglomeration characteristics of various oxide inclusions in molten steel containing rare earth element under different deoxidation conditions, *ISIJ Int.*, 61(2021), No. 5, p. 1396.
[47] H. Hasegawa, K. Nakajima, and S. Mizoguchi, "*In-situ*" observation of phase transformation and MnS precipitation in Fe–Si alloys, *Tetsu- to-Hagane*, 87(2001), No. 6, p. 433.
[48] P.C. Yan, M.X. Guo, and B. Blanpain, *In situ* observation of the formation and interaction behavior of the oxide/oxysulfide inclusions on a liquid iron surface, *Metall. Mater. Trans. B*, 45(2014), No. 3, p. 903.
[49] C.G. Aneziris, C. Schroeder, M. Emmel, G. Schmidt, H.P. Heller, and H. Berek, *In situ* observation of collision between exogenous and endogenous inclusions on steel melts for active steel filtration, *Metall. Mater. Trans. B*, 44(2013), No. 4, p. 954.
[50] W.Z. Mu, N. Dogan, and K.S. Coley, *In situ* observations of agglomeration of non-metallic inclusions at steel/Ar and steel/slag interfaces by high-temperature confocal laser scanning microscope: A review, *JOM*, 70(2018), No. 7, p. 1199.
[51] S. Vantilt, B. Coletti, B. Blanpain, J. Fransaer, P. Wollants, and S. Sridhar, Observation of inclusions in manganese-silicon killed steels at steel–gas and steel–slag interfaces, *ISIJ Int.*, 44(2004), No. 1, p. 1.
[52] W.Z. Mu, N. Dogan, and K.S. Coley, Agglomeration of non-metallic inclusions at steel/Ar interface: *In situ* observation experiments and model validation, *Metall. Mater. Trans. B*, 48(2017), No. 5, p. 2379.
[53] W.Z. Mu, N. Dogan, and K.S. Coley, Agglomeration of non-metallic inclusions at the steel/Ar interface: Model application, *Metall. Mater. Trans. B*, 48(2017), No. 4, p. 2092.
[54] W.Z. Mu, N. Dogan, and K.S. Coley, *In situ* observation of deformation behavior of chain aggregate inclusions: A case study for Al_2O_3 at a liquid steel/argon interface, *J. Mater. Sci.*, 53(2018), No. 18, p. 13203.
[55] R. Chen, Z.P. Chen, Y.T. Xu, C.D. Zhou, and D. Shu, *In-situ* observation of behaviors of inclusions in bearing steel, *J. Iron. Steel Res. Int.*, 27(2015), No. 12, p. 48.
[56] M. Jiang, X.H. Wang, J.J. Pak, and P. Yuan, *In situ* observation on behaviors of CaO–MgO–Al_2O_3–SiO_2 complex inclusions at solid–liquid interface of low-oxygen special steel, *Metall. Mater. Trans. B*, 45(2014), No. 5, p. 1656.
[57] Y. Kang, B. Sahebkar, P.R. Scheller, K. Morita, and S.C. Du, Observation on physical growth of nonmetallic inclusion in liquid steel during ladle treatment, *Metall. Mater. Trans. B*, 42(2011), No. 3, p. 522.
[58] Q.R. Tian, G.C. Wang, D.L. Shang, *et al.*, *In situ* observation of the precipitation, aggregation, and dissolution behaviors of TiN inclusion on the surface of liquid GCr15 bearing steel, *Metall. Mater. Trans. B*, 49(2018), No. 6, p. 3137.
[59] W.Z. Mu and C.J. Xuan, Agglomeration mechanism of complex Ti–Al oxides in liquid ferrous alloys considering high-temperature interfacial phenomenon, *Metall. Mater. Trans. B*, 50(2019), No. 6, p. 2694.
[60] M.H. Wu, Y. Ren, and L.F. Zhang, *In-situ* observation of collision and agglomeration of La_2O_3–La_2S_3 inclusions on surface of molten 304 stainless steels, *Metall. Mater. Trans. B*, 55(2024), No. 4, p. 2324.
[61] H.Y. Mu, T.S. Zhang, L. Yang, R.R. Xavier, R.J. Fruehan, and B.A. Webler, *In situ* observation of MgO inclusions in liquid iron-aluminum alloys, *Metall. Mater. Trans. B*, 47(2016), No. 6, p. 3375.
[62] P. Misra, V. Chevrier, S. Sridhar, and A.W. Cramb, *In situ* observations of inclusions at the (Mn, Si)-killed steel/CaO–Al_2O_3 interface, *Metall. Mater. Trans. B*, 31(2000), No. 5, p. 1135.
[63] S.K. Michelic, U. Dieguez Salgado, and C. Bernhard, *In-situ* observation of the behaviour of non-metallic inclusions at different interfaces in the system steel–slag–refractory, *IOP Conf. Ser. Mater. Sci. Eng.*, 143(2016), art. No. 012010.
[64] Q. Yue, H.H. Chen, C.H. Yao, D. Lu, J.F. Zhang, and F. Huang, Review of collision and growth on non-metallic inclusion in steel, *J. Iron Steel Res.*, 24(2012), No. 9, p. 1.
[65] L.M. Cheng, L.F. Zhang, and P. Shen, Fundamentals of interfacial wettability in ironmaking and steelmaking, *Chin. J. Eng.*, 40(2018), No. 12, p. 1434.
[66] M. Valdez, K. Prapakorn, A.W. Cramb, and S. Sridhar, Dissolution of alumina particles in CaO–Al_2O_3–SiO_2–MgO slags, *Ironmaking Steelmaking*, 29(2002), No. 1, p. 47.
[67] K.W. Yi, C. Tse, J.H. Park, M. Valdez, A.W. Cramb, and S. Sridhar, Determination of dissolution time of Al_2O_3 and MgO inclusions in synthetic Al_2O_3–CaO–MgO slags, *Scand. J. Metall.*, 32(2003), No. 4, p. 177.
[68] B.J. Monaghan, L. Chen, and J. Sorbe, Comparative study of oxide inclusion dissolution in CaO–SiO_2–Al_2O_3 slag, *Ironmaking Steelmaking*, 32(2005), No. 3, p. 258.
[69] J.H. Park, I.H. Jung, and H.G. Lee, Dissolution behavior of Al_2O_3 and MgO inclusions in the CaO–Al_2O_3–SiO_2 slags: Formation of ring-like structure of $MgAl_2O_4$ and Ca_2SiO_4 around MgO inclusions, *ISIJ Int.*, 46(2006), No. 11, p. 1626.
[70] J. Liu, M. Guo, P.T. Jones, F. Verhaeghe, B. Blanpain, and P. Wollants, *In situ* observation of the direct and indirect dissolution of MgO particles in CaO–Al_2O_3–SiO_2-based slags, *J. Eur. Ceram. Soc.*, 27(2007), No. 4, p. 1961.
[71] J.H. Liu, F. Verhaeghe, M.X. Guo, B. Blanpain, and P. Wollants, *In situ* observation of the dissolution of spherical alumina particles in CaO–Al_2O_3–SiO_2 melts, *J. Am. Ceram. Soc.*, 90(2007), No. 12, p. 3818.
[72] S. Feichtinger, S.K. Michelic, Y.B. Kang, and C. Bernhard, *In situ* observation of the dissolution of SiO_2 particles in CaO–Al_2O_3–SiO_2 slags and mathematical analysis of its dissolution pattern, *J. Am. Ceram. Soc.*, 97(2014), No. 1, p. 316.
[73] S. Michelic, J. Goriupp, S. Feichtinger, Y.B. Kang, C. Bernhard, and J. Schenk, Study on oxide inclusion dissolution in secondary steelmaking slags using high temperature confocal scanning laser microscopy, *Steel Res. Int.*, 87(2016), No. 1, p. 57.
[74] T.L. Tian, Y.Z. Zhang, H.H. Zhang, K.X. Zhang, J. Li, and H. Wang, Dissolution behavior of SiO_2 in the molten blast fur-

nace slags, *Int. J. Appl. Ceram. Technol.*, 16(2019), No. 3, p. 1078.

[75] X. Guo, Z.H.I. Sun, J. Van Dyck, M. Guo, and B. Blanpain, *In Situ*Observation on lime dissolution in molten metallurgical slags–kinetic aspects, *Ind. Eng. Chem. Res.*, 53(2014), No. 15, p. 6325.

[76] B.J. Monaghan and L. Chen, Dissolution behavior of alumina micro-particles in CaO–SiO_2–Al_2O_3 liquid oxide, *J. Non Cryst. Solids*, 347(2004), No. 1-3, p. 254.

[77] B.J. Monaghan and L.Chen, Effect of changing slag composition on spinel inclusion dissolution, *Ironmaking Steelmaking*, 33(2006), No. 4, p. 323.

[78] K.Y. Miao, A. Haas, M. Sharma, W.Z. Mu, and N. Dogan, *In situ* observation of calcium aluminate inclusions dissolution into steelmaking slag, *Metall. Mater. Trans. B*, 49(2018), No. 4, p. 1612.

[79] M. Sharma, W.Z. Mu, and N. Dogan, *In situ* observation of dissolution of oxide inclusions in steelmaking slags, *JOM*, 70(2018), No. 7, p. 1220.

[80] Y. Ren, P. Zhu, C.Y. Ren, N. Liu, and L.F. Zhang, Dissolution of SiO_2 inclusions in CaO–SiO_2-based slags *in situ* observed using high-temperature confocal scanning laser microscopy, *Metall. Mater. Trans. B*, 53(2022), No. 2, p. 682.

[81] A.B. Fox, M.E. Valdez, J. Gisby, R.C. Atwood, P.D. Lee, and S. Sridhar, Dissolution of ZrO_2, Al_2O_3, MgO and $MgAl_2O_4$ particles in a B_2O_3 containing commercial fluoride-free mould slag, *ISIJ Int.*, 44(2004), No. 5, p. 836.

[82] B.J. Monaghan, S.A. Nightingale, L. Chen, and G. Brooks, The dissolution behavior of selected oxides in CaO–SiO_2–Al_2O_3 slags, [in] *Conf. Molten Slag Fluxes and Salts-The South African Institute of Mining and Metallurgy*, Johannesburg, 2004, p. 585.

[83] F. Verhaeghe, J. Liu, M. Guo, S. Arnout, B. Blanpain, and P. Wollants, Dissolution and diffusion behavior of Al_2O_3 in a CaO–Al_2O_3–SiO_2 liquid: An experimental-numerical approach, *Appl. Phys. Lett.*, 91(2007), No. 12, art. No. 124104.

[84] J.H. Park, J.G. Park, D.J. Min, Y.E. Lee, and Y.B. Kang, *In situ* observation of the dissolution phenomena of SiC particle in CaO–SiO_2–MnO slag, *J. Eur. Ceram. Soc.*, 30(2010), No. 15, p. 3181.

[85] Z.H.I. Sun, X.L. Guo, J. Van Dyck, M.X. Guo, and B. Blanpain, Phase evolution and nature of oxide dissolution in metallurgical slags, *AlChE. J.*, 59(2013), No. 8, p. 2907.

[86] Y.M. Lee, J.K. Yang, D.J. Min, and J.H. Park, Mechanism of MgO dissolution in MgF_2–CaF_2–MF (M=Li or Na) melts: Kinetic analysis via *in situ* high temperature confocal scanning laser microscopy (HT-CSLM), *Ceram. Int.*, 45(2019), No. 16, p. 20251.

[87] M. Sharma and N. Dogan, Dissolution behavior of aluminum titanate inclusions in steelmaking slags, *Metall. Mater. Trans. B*, 51(2020), No. 2, p. 570.

[88] Y.J. Park, Y.M. Cho, W.Y. Cha, and Y.B. Kang, Dissolution kinetics of alumina in molten CaO–Al_2O_3–FetO–MgO–SiO_2 oxide representing the RH slag in steelmaking process, *J. Am. Ceram. Soc.*, 103(2020), No. 3, p. 2210.

[89] C.Y. Ren, C.D. Huang, L.F. Zhang, and Y. Ren, *In situ* observation of the dissolution kinetics of Al_2O_3 particles in CaO–Al_2O_3–SiO_2 slags using laser confocal scanning microscopy, *Int. J. Miner. Metall. Mater.*, 30(2023), No. 2, p. 345.

[90] L. Gou, H. Liu, Y. Ren, and L.F. Zhang, Concept of inclusion capacity of slag and its application on the dissolution of Al_2O_3, ZrO_2 and SiO_2 inclusions in CaO–Al_2O_3–SiO_2 slag, *Metall. Mater. Trans. B*, 54(2023), No. 3, p. 1314.

[91] L.F. Zhang and Y. Ren, Concept of inclusion capacity of slag and its application, *Iron Steel*, 58(2023), No. 2, p. 47.

[92] Y.G. Wang and C.J. Liu, *In situ* observation of transient evolution of inclusions by Ca treatment in molten steel, *Metall. Mater. Trans. B*, 53(2022), No. 5, p. 2768.

[93] G.J. Chen, Y. Ren, M.H. Wu, W.J. Wang, and L.F. Zhang, *In-situ* observation of the modification behavior of alumina inclusions in a calcium-treated steel, *ISIJ Int.*, 64(2024), No. 8, p. 1263.

[94] Y. Wang, S. Sridhar, and M. Valdez, Formation of CaS on Al_2O_3–CaO inclusions during solidification of steels, *Metall. Mater. Trans. B*, 33(2002), No. 4, p. 625.

[95] M.E. Valdez, Y. Wang, and S. Sridhar, MnS precipitation behavior in re-sulfurized steels with intermediate levels of sulfur, *Steel Res. Int.*, 76(2005), No. 4, p. 306.

[96] K. Nakama, Y. Haruna, J. Nakano, and S. Sridhar, The effect of alloy solidification path on sulfide formation in Fe–Cr–Ni alloys, *ISIJ Int.*, 49(2009), No. 3, p. 355.

[97] Y.Z. Luo, J.M. Zhang, Z.M. Liu, and C. Xiao, In situ observation and thermodynamic calculation of MnS in 49MnVS3 non-quenched and tempered steel, *Acta Metall. Sin. Engl. Lett.*, 24(2011), No. 4, p. 326.

[98] D.L. Hu, H. Liu, J.B. Xie, J. Cheng, J. Li, and J.X. Fu, Analysis of precipitation behavior of MnS in sulfur-bearing steel system with finite-difference segregation model, *J. Iron Steel Res. Int.*, 25(2018), No. 8, p. 803.

[99] Q.R. Tian, G.C. Wang, X.H. Yuan, Q. Wang, and S. Sridhar, Complex precipitates of TiN–MC_x in GCr15 bearing steel, *Metals*, 9(2019), No. 6, art. No. 641.

[100] Y. Tanaka, F. Pahlevani, S.C. Moon, R. Dippenaar, and V. Sahajwalla, *In situ* characterisation of MnS precipitation in high carbon steel, *Sci. Rep.*, 9(2019), No. 1, art. No. 10096.

[101] J. Zeng, C.Y. Zhu, W.L. Wang, and X. Li, *In situ* observation of the MnS precipitation behavior in high-sulfur microalloyed steel under different cooling rates, *Metall. Mater. Trans. B*, 51(2020), No. 6, p. 2522.

[102] P. Shen, H. Zhang, X.Y. Xu, Q.K. Yang, and J.X. Fu, Study on the high-temperature evolution and formation mechanism of inclusions in Te-treated resulfurized special steel, *Steel Res. Int.*, 92(2021), No. 11, art. No. 2100235.

[103] J.H. Chu, L.Q. Zhang, J. Yang, Y.P. Bao, N. Ali, and C.J. Zhang, Characterization of precipitation, evolution, and growth of MnS inclusions in medium/high manganese steel during solidification process, *Mater. Charact.*, 194(2022), art. No. 112367.

[104] L. Cao, G.C. Wang, Y.Y. Xiao, and R.G. Yang, Effect of Mg addition on TiN inclusions in GCr15 bearing steel, *J. Iron Steel Res. Int.*, 29(2022), No. 6, p. 925.

[105] H. Liu, W.F. Li, C.Y. Ren, L.F. Zhang, and Y. Ren, Inclusion evolution in Al-killed Ca-treated steels at heat treatment temperature *in situ* observed using confocal scanning laser microscope, *Metall. Mater. Trans. B*, 53(2022), No. 3, p. 1323.

[106] X.L. Zhu, J. Yang, S. Wang, *et al*., The investigation of precipitation behavior of titanium compounds for high titanium steel based on *in situ* observation, *PLoS One*, 18(2023), No. 4, art. No. e0275049.

[107] L. Cao, G.C. Wang, Y.Y. Xiao, Z. Zhao, and J.G. Li, *In situ* observation of the evolution behavior of MnS inclusions in high-Al medium-Mn steel, *Metall. Mater. Trans. B*, 55(2024), No. 2, p. 660.

[108] X.J. Shao, X.H. Wang, M. Jiang, W.J. Wang, and F.X. Huang, Effect of heat treatment conditions on shape control of large-sized elongated MnS inclusions in resulfurized free-cutting steels, *ISIJ Int.*, 51(2011), No. 12, p. 1995.

[109] X.J. Shao, X.H. Wang, M. Jiang, W.J. Wang, F.X. Huang, and Y.Q. Ji, *In situ* observation of MnS inclusion behavior in resulfurized free-cutting steel during heating, *Acta Metall. Sin.*,

47(2011), No. 9, p. 1210.
[110] Q.Y. Wang, X.D. Zou, H. Matsuura, and C. Wang, Evolution of inclusions during the 1473 K (1200°C) heating process of EH36 shipbuilding steel, *Metall. Mater. Trans. B*, 49(2018), No. 1, p. 18.
[111] Q.Y. Wang, X.D. Zou, H. Matsuura, and C. Wang, Evolution of inclusions during 1473 K heating process in EH36 shipbuilding steel with Mg addition, *JOM*, 70(2018), No. 4, p. 521.
[112] H.P. Wang, B. Bai, S.L. Jiang, L.F. Sun, and Y. Wang, An *in situ* study of the formation of rare earth inclusions in arsenic high carbon steels, *ISIJ Int.*, 59(2019), No. 7, p. 1259.
[113] P.S. Song, Y.Q. Li, T.H. Zhu, and L.F. Zhang, *In situ* observation on the heterogeneous nucleation of MnS in heavy rail steels with varied aluminum content, *Steel Res. Int.*, 94(2023), No. 5, art. No. 2200684.
[114] H. Hasegawa, K. Nakajima, and S. Mizoguchi, Effects of MnS on the heterogeneous nucleation of Cu precipitates in Fe–10 and –5mass% Cu alloys, *ISIJ Int.*, 43(2003), No. 7, p. 1021.
[115] K.I. Yamamoto, H. Shibata, K. Nakajima, and S. Mizoguchi, Precipitation behavior of Cu and MnS at high temperature in Fe–10mass%Cu alloys, *Tetsu-to-Hagane*, 90(2004), No. 10, p. 781.
[116] H.B. Yin and T. Emi, Marangoni flow at the gas/melt interface of steel, *Metall. Mater. Trans. B*, 34(2003), No. 5, p. 483.
[117] S.Y. Chen, X.D. Yue, G.C. Jin, Q.C. Li, and G.W. Chang, Behavior of inclusions in process of solid growth during solidification of Fe–0.15C–0.8Mn steel, *J. Iron Steel Res. Int.*, 19(2012), No. 5, p. 17.
[118] C.L. Yan, F.M. Wang, W.L. Mo, P.C. Xiao, and Q.J. Zhang, Migration behavior of inclusions at the solidification front in oxide metallurgy, *Materials*, 16(2023), No. 12, art. No. 4486.
[119] X.J. Shao, X.H. Wang, C.X. Ji, H.B. Li, Y. Cui, and G.S. Zhu, Morphology, size and distribution of MnS inclusions in non-quenched and tempered steel during heat treatment, *Int. J. Miner. Metall. Mater.*, 22(2015), No. 5, p. 483.
[120] J. Yang, K. Zhu and G. wang, Progress in the technological development of oxide metallurgy for manufacturing steel plates with excellent HAZ toughness, *Baosteel Tech. Res*., 2008, No. 2, p. 43.
[121] Y. Kitani, R. Ikeda, K. Yasuda, K. Oi, and K. Ichimiya, Improvement of HAZ toughness for high heat input welding by using boron diffusion from weld metal, *Weld. World*, 51(2007), No. 1, p. 31.
[122] H. Duan, Y.Y. Shan, K. Yang, X.B. Shi, W. Yan, and Y. Ren, Experimental on process, microstructure and mechanical properties of X80 high strength pipeline steel for low temperature, *Iron Steel*, 55(2020), No. 2, p. 103.
[123] Z.Y. Zou, S.T. Han, Y.X. Li, and C. Wang, Analysis of internal mechanism of impact toughness of CGHAZ for high heat input welding steels, *China Metall.*, 29(2019), No. 1, p. 18.
[124] B.X. Wang, F.X. Zhu, C. Wang, H.N. Lou, Z.D. Wang, and G.D. Wang, Application of oxide metallurgy in high heat input welding steels, *Iron Steel*, 54(2019), No. 9, p. 12.
[125] B.X. Wang, Z.Z. Wu, H.N. Lou, C. Wang, Z.D. Wang, and G.D. Wang, Effect of oxide metallurgy on microstructure and properties of HAZ in EH36 steel, *J. Iron Steel Res.*, 31(2019), No. 2, p. 239.
[126] W.Z. Mu, P. Hedström, H. Shibata, P.G. Jönsson, and K. Nakajima, High-temperature confocal laser scanning microscopy studies of ferrite formation in inclusion-engineered steels: A review, *JOM*, 70(2018), No. 10, p. 2283.
[127] H. Terasaki, T. Yamada, and Y.I. Komizo, *In-situ* observation of nucleation and growth of acicular ferrite in weld metal, *Tetsu-to-Hagane*, 93(2007), No. 1, p. 27.
[128] D. Zhang, H. Terasaki, and Y.I. Komizo, *In situ* observation of the formation of intragranular acicular ferrite at non-metallic inclusions in C–Mn steel, *Acta Mater.*, 58(2010), No. 4, p. 1369.
[129] Z.Y. Hu, C.W. Yang, M. Jiang, G.W. Yang, W.J. Wang, and X.H. Wang, *In situ* observation of intragranular acicular ferrite nucleated on complex titanium containing inclusions in titanium deoxidized steel, *Acta Metall. Sin.*, 47(2011), No. 8, p. 971.
[130] X.L. Wan, K.M. Wu, G. Huang, and R. Wei, *In situ* observations of the formation of fine-grained mixed microstructures of acicular ferrite and bainite in the simulated coarse-grained heated-affected zone, *Steel Res. Int.*, 85(2014), No. 2, p. 243.
[131] X.L. Wan, R. Wei, L. Cheng, M. Enomoto, and Y. Adachi, Lengthening kinetics of ferrite plates in high-strength low-carbon low alloy steel, *J. Mater. Sci.*, 48(2013), No. 12, p. 4345.
[132] W.Z. Mu, P.G. Jönsson, and K. Nakajima, Effect of sulfur content on inclusion and microstructure characteristics in steels with Ti_2O_3 and TiO_2 additions, *ISIJ Int.*, 54(2014), No. 12, p. 2907.
[133] M. Jiang, X.H. Wang, Z.Y. Hu, K.P. Wang, C.W. Yang, and S.R. Li, Microstructure refinement and mechanical properties improvement by developing IAF on inclusions in Ti–Al complex deoxidized HSLA steel, *Mater. Charact.*, 108(2015), p. 58.
[134] X.L. Wan, K.M. Wu, L. Cheng, and R. Wei, *In-situ* observations of acicular ferrite growth behavior in the simulated coarse-grained heat-affected zone of high-strength low-alloy steels, *ISIJ Int.*, 55(2015), No. 3, p. 679.
[135] Z.H. Wu, W. Zheng, G.Q. Li, H. Matsuura, and F. Tsukihashi, Effect of inclusions' behavior on the microstructure in Al–Ti deoxidized and magnesium-treated steel with different aluminum contents, *Metall. Mater. Trans. B*, 46(2015), No. 3, p. 1226.
[136] W.Z. Mu, H. Shibata, P. Hedström, P.G. Jönsson, and K. Nakajima, Ferrite formation dynamics and microstructure due to inclusion engineering in low-alloy steels by Ti_2O_3 and TiN addition, *Metall. Mater. Trans. B*, 47(2016), No. 4, p. 2133.
[137] C.K. Lin, Y.C. Pan, W.S. Hwang, *et al.*, *In situ* observation of growth behaviour of acicular ferrite in low-carbon steel containing 13 ppm magnesium, *Ironmaking Steelmaking*, 46(2019), No. 2, p. 176.
[138] D.Loder and S.K. Michelic, Systematic investigation of acicular ferrite formation on laboratory scale, *Mater. Sci. Technol.*, 33(2017), No. 2, p. 162.
[139] Y.K. Yang, D.P. Zhan, H. Lei, *et al.*, *In situ* observation of acicular ferrite nucleation and growth at different cooling rate in Ti–Zr deoxidized steel, *Metall. Mater. Trans. B*, 50(2019), No. 6, p. 2536.
[140] X. Wang, C. Wang, J. Kang, G. Yuan, R.D.K. Misra, and G.D. Wang, An *in situ* microscopy study on nucleation and growth of acicular ferrite in Ti–Ca–Zr deoxidized low-carbon steel, *Mater. Charact.*, 165(2020), art. No. 110381.
[141] T.T. Wang, S.F. Yang, J.S. Li, H. Guo, and Z.Y. Chen, Effect of *in situ* observation of cooling rates on acicular ferrite nucleation, *High Temp. Mater. Process.*, 41(2022), No. 1, p. 181.
[142] D.K. Liu, J. Yang, and Y.H. Zhang, *In-situ* observation of bainite transformation in CGHAZ of 420 MPa grade offshore engineering steel with different Mo contents, *ISIJ Int.*, 62(2022), No. 4, p. 714.
[143] H. Yao, Q. Ren, W. Yang, and L.F. Zhang, *In situ* observation and prediction of the transformation of acicular ferrites in Ti-containing HLSA steel, *Metall. Mater. Trans. B*, 53(2022), No. 3, p. 1827.
[144] X. Xie, M. Zhong, P.F. Zhao, H. Yu, and C. Wang, *In situ* observation of phase transformations in the weld metal of EH420

shipbuilding steel subjected to varied heat inputs, *Metall. Mater. Trans. A*, 54(2023), No. 7, p. 2532.

[145] Y.S. Li, Y.W. Dong, Z.H. Jiang, Q.F. Tang, S.Y. Du, and Z.W. Hou, Influence of rare earth Ce on hot deformation behavior of as-cast $Mn_{18}Cr18N$ high nitrogen austenitic stainless steel, *Int. J. Miner. Metall. Mater.*, 30(2023), No. 2, p. 324.

[146] W.N. Shi, S.F. Yang, and J.S. Li, Effect of nonmetallic inclusions on localized corrosion of spring steel, *Int. J. Miner. Metall. Mater.*, 28(2021), No. 3, p. 390.

[147] Q.K. Yang, P. Shen, D. Zhang, Y.X. Wu, and J.X. Fu, Analysis on composition and inclusions of ballpoint pen tip steel, *Int. J. Miner. Metall. Mater.*, 25(2018), No. 4, p. 420.

[148] L. Lin, B.S. Li, G.M. Zhu, Y.L. Kang, and R.D. Liu, Effects of Nb on the microstructure and mechanical properties of 38MnB5 steel, *Int. J. Miner. Metall. Mater.*, 25(2018), No. 10, p. 1181.

[149] H.B. Li, Z.H. Jiang, H. Feng, H.C. Zhu, B.H. Sun, and Z. Li, Corrosion behavior of ferritic stainless steel with 15wt% chromium for the automobile exhaust system, *Int. J. Miner. Metall. Mater.*, 20(2013), No. 9, p. 850.

[150] Y.P. Zeng, H.M. Fan, and X.S. Xie, Effects of the shape and size of rectangular inclusions on the fatigue cracking behavior of ultra-high strength steels, *Int. J. Miner. Metall. Mater.*, 20(2013), No. 4, p. 360.

[151] C. Gu, W.Q. Liu, J.H. Lian, and Y.P. Bao, In-depth analysis of the fatigue mechanism induced by inclusions for high-strength bearing steels, *Int. J. Miner. Metall. Mater.*, 28(2021), No. 5, p. 826.

[152] M.W. Zhou and H. Yu, Effects of precipitates and inclusions on the fracture toughness of hot rolling X70 pipeline steel plates, *Int. J. Miner. Metall. Mater.*, 19(2012), No. 9, p. 805.